New Routes to Polymetallic Clusters: Fluoride-Based Tri-, Deca-, and Hexaicosametallic Mn^{III} Clusters and their Magnetic Properties

Leigh F. Jones,[a] Gopalan Rajaraman,[a] Jonathon Brockman,[b] Muralee Murugesu,[b] E. Carolina Sañudo,[b] Jim Raftery,[a] Simon J. Teat,[d] Wolfgang Wernsdorfer,[c] George Christou,[b] Euan K. Brechin,*[a] and David Collison*[a]

Abstract: The syntheses, structures and magnetic properties of three new Mn^{III} clusters, $[Mn_{26}O_{17}(OH)_8(OMe)_4F_{10}(bta)_{22}(MeOH)_{14}(H_2O)_2]$ (**1**), $[Mn_{10}O_6(OH)_2(bta)_8(py)_8F_8]$ (**2**) and $[NHEt_3]_2[Mn_3O(bta)_6F_3]$ (**3**), are reported (bta = anion of benzotriazole), thereby demonstrating the utility of MnF_3 as a new synthon in Mn cluster chemistry. The "melt" reaction (100 °C) between MnF_3 and benzotriazole (btaH, $C_6H_5N_3$) under an inert atmosphere, followed by dissolution in MeOH produces the cluster $[Mn_{26}O_{17}(OH)_8(OMe)_4F_{10}(bta)_{22}(MeOH)_{14}(H_2O)_2]$ (**1**) after two weeks. Complex **1** crystallizes in the triclinic space group $P\bar{1}$, and consists of a complicated array of metal tetrahedra linked by μ_3-O^{2-} ions, μ_3- and μ_2-OH^- ions, μ_2-MeO^- ions and μ_2-bta^- ligands. The "simpler" reaction between MnF_3 and btaH in boiling MeOH (50 °C) also produces complex **1**. If this reaction is repeated in the presence of pyridine, the decametallic complex $[Mn_{10}O_6(OH)_2(bta)_8(py)_8F_8]$ (**2**) is produced. Complex **2** crystallizes in the triclinic space group $P\bar{1}$ and consists of a "supertetrahedral" $[Mn^{III}_{10}]$ core bridged by six μ_3-O^{2-} ions, two μ_3-OH^- ions, four μ_2-F^- ions and eight μ_2-bta^- ions. The replacement of pyridine by triethylamine in the same reaction scheme produces the trimetallic species $[NHEt_3]_2[Mn_3O(bta)_6F_3]$ (**3**). Complex **3** crystallises in the monoclinic space group $P2_1/c$ and has a structure analogous to that of the basic metal carboxylates of general formula $[M_3O(RCO_2)_6L_3]^{0/+}$, which consists of an oxo-centred metal triangle with μ_2-bta^- ligands bridging each edge of the triangle and the fluoride ions acting as the terminal ligands. DC magnetic susceptibility measurements in the 300–1.8 K and 0.1–7 T ranges were investigated for all three complexes. For each, the value of $\chi_M T$ decreases with decreasing temperatures; this indicates the presence of dominant antiferromagnetic exchange interactions in **1**–**3**. For complex **1**, the low-temperature value of $\chi_M T$ is 10 $cm^3 K mol^{-1}$ and fitting of the magnetisation data gives $S=4$, $g=2.0$ and $D=-0.90$ cm^{-1}. For complex **2**, the value of $\chi_M T$ falls to a value of approximately 5.0 $cm^3 K mol^{-1}$ at 1.8 K, which is consistent with a small spin ground state. For the triangular complex **3**, the best fit to the experimental $\chi_M T$ versus T data was obtained for the following parameters: $J_a=-5.01$ cm^{-1}, $J_b=+9.16$ cm^{-1} and $g=2.00$, resulting in an $S=2$ spin ground state. DFT calculations on **3**, however, suggest an $S=1$ or $S=0$ ground state with $J_a=-2.95$ cm^{-1} and $J_b=-2.12$ cm^{-1}. AC susceptibility measurements performed on **1** in the 1.8–4.00 K range show the presence of out-of-phase AC susceptibility signals, but no peaks. Low-temperature single-crystal studies performed on **1** on an array of micro-SQUIDS show the time- and temperature-dependent hysteresis loops indicative of single-molecule magnetism behaviour.

Keywords: cluster compounds · density functional calculations · fluorides · magnetic properties · manganese · N ligands

Introduction

Many Mn-based clusters have been reported over the last 20 years for two main reasons: the first is biological in origin, because Mn is prominent in the active sites of many metallo-biomolecules.[1] The most commonly studied is the water-oxidising complex (WOC) of photosystem II (PS II), the species in plants (and cyanobacteria) that brings about the oxidation of water into dioxygen. The WOC is a tetranuclear Mn cluster of yet unknown structure.[2] Thus, numerous Mn_4 complexes have been synthesised as models to probe the structural changes and mechanistic processes occurring in PS II.[3] The second reason is the paramagnetic nature of Mn clusters, many of which exhibit large ground spin states

[a] L. F. Jones, G. Rajaraman, Dr. J. Raftery, Dr. E. K. Brechin, Dr. D. Collison
Department of Chemistry, The University of Manchester
Oxford Road, Manchester, M13 9PL (UK)
Fax: (+44) 161-275-4616
E-mail: euan.k.brechin@man.ac.uk
david.collison@man.ac.uk

[b] J. Brockman, Dr. M. Murugesu, E. C. Sañudo, Prof. G. Christou
Department of Chemistry, University of Florida
Gainesville, Florida 32611-7200 (USA)

[c] Dr. W. Wernsdorfer
Laboratoire Louis Néel-CNRS
38042 Grenoble, Cedex 9 (France)

[d] Dr. S. J. Teat
CCLRC Daresbury Laboratory
Daresbury, Warrington, Cheshire, WA4 4AD (UK)

Supporting information for this article is available on the WWW under http://www.chemeurj.org/ or from the author.

DOI: 10.1002/chem.200400301

(*S*). This, coupled with a large zero-field splitting parameter (*D*) (derived from the single-ion anisotropy of Mn^{III}), gives rise to the superparamagnetic-like property of a barrier to magnetisation relaxation, which can be observed as hysteresis loops in magnetisation versus DC field studies.[4] Therefore, these discrete molecules behave as magnets below their blocking temperatures and have been termed single-molecule magnets (SMMs).[5] One consequence of this phenomenon is the possibility of using single molecules as information-storage devices. The last ten years has seen many attempts to produce new SMMs in the same mould as the original SMM $[Mn_{12}O_{12}(OAc)_{16}(H_2O)_4]\cdot 4H_2O\cdot 2CH_3CO_2H$,[6] and this has led to the discovery of numerous SMMs ranging in nuclearity from 4 to 84.[7] The majority of SMMs reported to date have been clusters that contain Mn^{III} ions.[8] In each case, the clusters have been made, at least initially, by serendipitous assembly of Mn starting materials with flexible organic bridging ligands, such as carboxylates or alkoxides. Manganese clusters have often displayed unusually large spin ground states, especially with respect to other 3d transition metals, and large and negative magnetoanisotropies resulting from the presence of Jahn–Teller distorted Mn^{III} ions. However, this presents a synthetic problem: there are few "simple" readily available sources of Mn^{III}. This has resulted in the use of two alternative techniques: 1) the use of the basic metal carboxylates of general formula, $[M_3O(RCO_2)_6L_3]^{0/+}$, which can contain either two or three Mn^{III} ions, and 2) the oxidation of Mn^{II} salts with permanganate (MnO_4^-). Both of these techniques have been successful, particularly the former.[9] However, continual use of carboxylates will restrict the diversity of the products obtained and, as an alternative, we have begun to investigate the chemistry of MnF_3 with the proligand benzotriazole (btaH) and its derivatives.

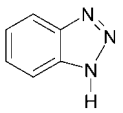

Benzotriazole has previously been used to produce model compounds for corrosion inhibition studies[10] and in M^{II} cluster chemistry;[11] however, until recently, it has never been used in the synthesis of M^{III} clusters.[12] Metal fluorides have been used to good effect in the synthesis of polymetallic chromium carboxylates[13] and, to a lesser extent, of Fe^{III} clusters, including the synthesis of an open-shell Keggin iron ion,[14] but have thus far rarely been used in manganese cluster chemistry.[15] The main disadvantage of the use of metal fluorides is their relative insolubility and therefore the apparent need for more "complicated" synthetic procedures. Indeed, the majority of fluoride-containing clusters have been isolated at elevated temperatures.[16] We have previously reported the synthesis of a $[Mn_{26}]$ cage from MnF_3 in a preliminary communication.[15] Herein we report an improved synthesis of this cluster and "simple" new routes to other large Mn^{III} clusters by the use of MnF_3.

Results and Discussion

Synthesis: In order to overcome the relative insolubility of MnF_3 in common organic solvents, our initial approach was to react MnF_3 in a "melt" reaction. Here the MnF_3 and the organic ligand (btaH) are mixed together and heated, under nitrogen or argon, to the melting point of the organic ligand (100 °C). As the ligand melts, the MnF_3 dissolves and the reaction proceeds. The resultant solid mixture can then be extracted into various solvents and crystallised. Complex **1** was synthesised by extracting this solid mixture into MeOH and diffusing Et_2O into the filtered solution over a period of two weeks. A simpler route to the same product was subsequently found: reaction of MnF_3 and btaH in boiling MeOH for 10 minutes, followed by filtration of the hot solution and Et_2O diffusion produces complex **1** in a larger yield. The repetition of this process in the presence of pyridine produces the decametallic complex **2**. The replacement of pyridine with triethylamine produces the trimetallic complex **3**.

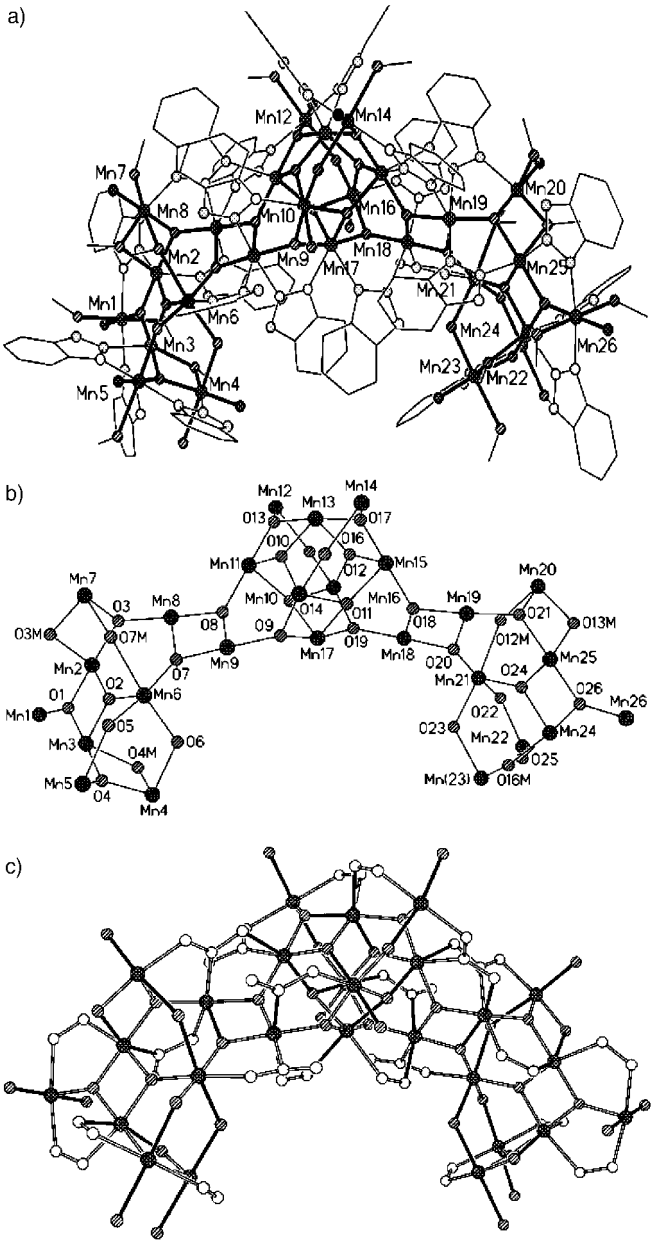

Figure 1. Top: Structure of complex **1**. Middle: Core of complex **1**. Bottom: Core of complex **1** showing the positions of the Jahn–Teller axes.

Some broad conclusions can be drawn from the above observations. The reaction performed with no base produces the largest cluster (**1**) with the lowest Mn/F ratio and was isolated in the lowest yield. The introduction of a weakly coordinating base (py, pK_a = 5.25) produces the second largest cluster (**2**), and the introduction of a strong non-coordinating base (NEt_3, pKa = 11.01), which also acts as a cation on protonation, produces the smallest cluster (**3**) in the largest yield. As in most cases of Mn cluster chemistry, it is extremely unlikely that complexes **1**–**3** are the only ones present in solution at any one given time. Thus the loss of F^- ions and the appearance of OH^-, O^{2-} and MeO^- ions, is also likely to involve the deprotonation/protonation, structural rearrangements and redox chemistry of other species present in solution. However, complexes **1**–**3** can all be described as aggregated triangular $\{Mn_3O\}$ units: complex **3** consists of one triangular unit, **2** is made from eight edge-sharing units and **1** contains twenty such units. This perhaps suggests that complex **3**, in the form $[Mn_3O(bta)_6F_3]^{2-}$, may be present in all of the above solutions, and that the identity of the isolated crystalline product is then dependent on the base or counterion added. When NEt_3 is added, complex **3** is isolated instantly in high yield, as it not only deprotonates the btaH ligands, but the resultant cations $[HNEt_3]^+$ stabilize the complex. Pyridinium ions, on the other hand, are "poor" cations (in crystallisation terms); however, pyridine molecules are frequently seen to act as terminal ligands in Mn^{III} clusters. This allows time for the hydrolysis and aggregation of the $\{Mn_3O(bta)_6F_3\}$ units into larger fragments, crystallizing as complex **2** after one week in a comparatively moderate yield. When no base is added (and thus there is no direct deprotonation of the btaH ligands) the hydrolysis process takes even longer (~2 weeks), and complex **1** crystallizes, albeit in a poor yield.

Table 1. Crystal data and structure refinement for complexes **1**–**3**.

	1 $[Mn_{26}]$	**2** $[Mn_{10}]$	**3** $[Mn_3]$
formula	$C_{151.50}H_{196}F_{10}Mn_{26}N_{66}O_{46.50}$	$C_{92.40}H_{83.60}F_8Mn_{10}N_{33.50}O_{10.15}$	$C_{50}H_{64}F_3Mn_3N_{20}O_3$
M [g mol^{-1}]	5304.18	2527.13	1215.03
crystal size [mm]	0.08 × 0.04 × 0.01	0.18 × 0.08 × 0.04	0.30 × 0.20 × 0.01
crystal habit	plates	plates	plates
colour	orange/brown	orange/brown	green
crystal system	triclinic	triclinic	monoclinic
space group	$P\bar{1}$	$P\bar{1}$	$P2_1/c$
a [Å]	17.9570(10)	17.5090(12)	21.440(2)
b [Å]	24.0865(14)	18.1168(13)	12.5632(12)
c [Å]	27.3871(16)	18.6737(13)	20.0675(19)
α [°]	98.907(2)	90.541(2)	90
β [°]	95.758(2)	99.171(2)	91.643(2)
γ [°]	101.778(2)	98.173(2)	90
V [Å^3]	11349.2(11)	5785.2(7)	5403.0(9)
T [K]	150(2)	150(2)	100(2)
Z	2	2	4
$2\theta_{max}$	40.14	40.14	57.28
ρ_{calcd} [g cm^{-3}]	1.552	1.451	1.494
μ [mm^{-1}]	1.48	1.131	0.764
data collected	37727	37509	42491
unique data	23486 (R_{int} = 0.0521)	19469 (R_{int} = 0.0761)	12792 (R_{int} = 0.0743)
unique data [$I > 2\sigma(F)$]	13934	13582	7057
$R1$, $wR2$	0.0786, 0.2218	0.0761, 0.2490	0.0417, 0.0717
goodness of fit	1.019	1.042	0.798

Attempts to interconvert **1**–**3** have proved unsuccessful so far. For example, dissolution of **3** in a MeOH/py solution does not result in the isolation of complex **2**. This investigation continues, however.

Crystal structures: The structure of $[Mn_{26}O_{17}(OH)_8(OMe)_4F_{10}(bta)_{22}(MeOH)_{14}(H_2O)_2]$ (**1**) is shown in Figure 1 (top), the crystal data are given in Table 1 and selected bond lengths are given in Table 2. A complete list of angles is available in the Supporting Information (Table S1). The $[Mn^{III}_{26}O_{17}(OH)_8(OMe)_4]^{32+}$ core of **1** (Figure 1, middle) can be described as a central distorted tetraface-capped octahedron (Mn9–Mn18), either side of which are attached two vertex-sharing tetrahedra (Mn2–Mn8 and Mn19–Mn25), centred on Mn6 and Mn21. A pseudo-C_2 axis passes through the direction defined by Mn13 and Mn17, situated at the "top" of the molecule. The O^{2-} ions all bridge in their usual μ_3-fashion to form $\{Mn_3O\}^{7+}$ units. The OH^- ions are of two types: four are μ_3-bridging (O10, O11, O14, O16) and are situated within the tetraface-capped octahedron, while the remaining ions are μ_2-bridging (O5, O6, O12, O15, O22, O23) and are situated both in the tetraface-capped octahedron (O12 and O15) and within the two vertex-sharing tetrahedra (O5, O6, O22 and O23). The 22 deprotonated bta^- ligands are of two types: four use all three nitrogen atoms to bond to three Mn^{III} centres, while the remaining eighteen use only two nitrogen atoms to bond to two Mn^{III} centres, the third nitrogen atom forms hydrogen bonds to adjacent MeOH, H_2O or OH^- ligands. The four MeO^- ions are all μ_2-bridging; however, there are also two MeOH molecules that act as μ_2-bridges (O7M, O12M) between Mn6–Mn7 and Mn20–Mn21, respectively. In each case, the O atom of the MeOH molecule is not deprotonated, as confirmed by the observed bond lengths (2.393–2.476 Å), bond valence sum analysis (vide infra) and the presence of a hydrogen bond between each O atom and an unbound N atom of a μ_2-bridging bta^- ligand (e.g., O7M···N73, 2.738 Å). The ten F^- ions are all terminal with bond lengths ranging from 1.800(8) to 1.844(8) Å. The Mn centres all lie in distorted octahedral geometries and display the Jahn–Teller elongations expected for high-spin Mn^{III}, although these axes are not co-parallel (Figure 1, bottom). The MeOH solvent molecule is hydrogen-bonded to an MeOH molecule attached to the $[Mn_{26}]$ core (O1S···O9M, 2.806 Å) and to an unbound N atom of a μ_2-bta^- ligand (O1S···N53, 2.819 Å). The oxidation states of both the metal and non-metal ions were deter-

Table 2. Selected interatomic distances [Å] for **1**.

Mn1–F1	1.800(7)	Mn1–O1	1.867(7)	Mn1–N21	2.054(11)	Mn1–N11	2.058(11)
Mn1–O2M	2.147(9)	Mn1–O1M	2.176(9)	Mn2–O1	1.878(8)	Mn2–O2	1.902(8)
Mn2–O3	1.905(8)	Mn2–N12	2.102(10)	Mn2–O3M	2.194(8)	Mn2–N42	2.228(10)
Mn2–Mn3	2.872(3)	Mn2–Mn7	3.033(3)	Mn3–O1	1.878(8)	Mn3–O2	1.913(8)
Mn3–O4	1.920(8)	Mn3–N22	2.106(12)	Mn3–O4M	2.194(9)	Mn3–N32	2.259(11)
Mn3–Mn4	3.028(3)	Mn4–F2	1.839(9)	Mn4–O4M	1.891(9)	Mn4–O4	1.909(9)
Mn4–N52	2.065(15)	Mn4–O6	2.147(8)	Mn4–O1W	2.260(11)	Mn5–F3	1.813(10)
Mn5–O4	1.870(10)	Mn5–N31	2.016(11)	Mn5–N51	2.041(14)	Mn5–O5	2.103(8)
Mn5–O5M	2.231(13)	Mn6–O7	1.826(8)	Mn6–O5	1.873(7)	Mn6–O2	1.904(8)
Mn6–N61	2.055(10)	Mn6–O6	2.118(8)	Mn6–O7M	2.393(9)	Mn7–F4	1.812(7)
Mn7–O3M	1.867(8)	Mn7–O3	1.911(8)	Mn7–N81	2.027(10)	Mn7–O6M	2.260(10)
Mn7–O7M	2.476(9)	Mn8–O3	1.877(7)	Mn8–O8	1.888(7)	Mn8–N82	2.026(10)
Mn8–N41	2.055(10)	Mn8–O7	2.073(8)	Mn8–N91	2.428(10)	Mn8–Mn9	2.907(2)
Mn9–O7	1.851(7)	Mn9–O9	1.899(7)	Mn9–O8	1.914(8)	Mn9–N62	2.101(10)
Mn9–N72	2.257(10)	Mn9–N102	2.297(11)	Mn10–O9	1.863(8)	Mn10–O12	1.867(7)
Mn10–O11	1.960(7)	Mn10–O10	1.978(9)	Mn10–N71	2.092(11)	Mn10–O8M	2.121(10)
Mn10–Mn17	3.000(3)	Mn11–O13	1.904(9)	Mn11–O8	1.921(8)	Mn11–O10	1.942(8)
Mn11–N92	2.035(10)	Mn11–O14	2.121(7)	Mn11–N83	2.408(10)	Mn11–Mn13	2.949(3)
Mn12–F5	1.804(9)	Mn12–O13	1.876(10)	Mn12–N131	2.045(12)	Mn12–N93	2.080(11)
Mn12–O15	2.129(7)	Mn12–O9M	2.197(12)	Mn13–N12B	1.85(2)	Mn13–O13	1.915(9)
Mn13–O17	1.921(9)	Mn13–O10	2.005(9)	Mn13–O16	2.031(8)	Mn13–N132	2.090(13)
Mn13–N122	2.37(2)	Mn13–Mn15	2.946(3)	Mn14–F6′	1.792(13)	Mn14–F6	1.837(13)
Mn14–O17	1.865(11)	Mn14–N121	1.925(17)	Mn14–N171	2.042(13)	Mn14–O12	2.123(9)
Mn14–N12A	2.18(2)	Mn14–O10M	2.490(18)	Mn15–O17	1.891(9)	Mn15–O16	1.915(9)
Mn15–O18	1.919(7)	Mn15–N172	1.992(13)	Mn15–O11	2.146(8)	Mn15–N181	2.458(12)
Mn16–O19	1.863(8)	Mn16–O15	1.881(7)	Mn16–O16	1.969(9)	Mn16–O14	1.979(7)
Mn16–O11M	2.093(10)	Mn16–N141	2.108(11)	Mn16–Mn17	2.993(3)	Mn17–O9	1.968(7)
Mn17–O19	1.989(8)	Mn17–O14	2.101(8)	Mn17–O11	2.140(8)	Mn17–N111	2.192(10)
Mn17–N101	2.234(10)	Mn18–O20	1.850(7)	Mn18–O19	1.888(7)	Mn18–O18	1.917(8)
Mn18–N152	2.080(11)	Mn18–N142	2.259(11)	Mn18–N112	2.296(10)	Mn18–Mn19	2.894(3)
Mn19–O21	1.884(7)	Mn19–O18	1.889(7)	Mn19–O20	2.040(8)	Mn19–N182	2.070(11)
Mn19–N161	2.080(12)	Mn19–N173	2.377(13)	Mn20–F7	1.844(8)	Mn20–O13M	1.852(9)
Mn20–O21	1.907(9)	Mn20–N183	2.028(11)	Mn20–O14M	2.222(11)	Mn20–O12M	2.464(9)
Mn20–Mn25	3.029(3)	Mn21–O20	1.836(8)	Mn21–O22	1.883(7)	Mn21–O24	1.909(8)
Mn21–N151	2.062(11)	Mn21–O23	2.142(6)	Mn21–O12M	2.443(9)	Mn22–F8	1.816(9)
Mn22–O25	1.869(9)	Mn22–N19C	1.96(3)	Mn22–N221	2.007(14)	Mn22–N22A	2.05(2)
Mn22–O22	2.106(7)	Mn22–N192	2.114(17)	Mn22–O15M	2.219(12)	Mn23–F9	1.828(8)
Mn23–O16M	1.880(10)	Mn23–O25	1.903(8)	Mn23–N191	1.913(16)	Mn23–O23	2.112(7)
Mn23–O17M	2.281(10)	Mn23–N19B	2.32(3)	Mn23–Mn24	3.009(3)	Mn24–O26	1.895(8)
Mn24–O25	1.913(9)	Mn24–O24	1.926(8)	Mn24–N202	2.112(12)	Mn24–N22B	2.12(3)
Mn24–O16M	2.179(9)	Mn24–N222	2.321(16)	Mn24–Mn25	2.878(3)	Mn25–O26	1.871(9)
Mn25–O24	1.895(9)	Mn25–O21	1.900(8)	Mn25–N212	2.099(12)	Mn25–O13M	2.175(9)
Mn25–N162	2.226(12)	Mn26–F10	1.814(8)	Mn26–O26	1.870(8)	Mn26–N201	2.050(12)
Mn26–N211	2.054(12)	Mn26–O18M	2.172(10)	Mn26–O19M	2.177(10)		

mined by means of charge balance considerations, bond length analysis and bond valence sum (BVS) calculations (Table 3). All twenty six Mn ions are Mn^{III} ions. This is supported by the BVS analysis and the presence of Jahn–Teller elongation axes at each metal centre. Of the twenty μ_3-bridging single ions, sixteen give BVS values equal to 2 and were assigned as O^{2-}. Two (O11, O14) give BVS values equal to 1, and were assigned as OH^-. The remaining two ions (O10, O16) give intermediate BVS values of approximately 1.5, and bond lengths in the range 1.978–2.031 Å. These ions were assigned as half OH^- and half O^{2-}. Of the six μ_2-bridging single ions, four give BVS values equal to 1 and were assigned as OH^-. However, two (O6, O23) give intermediate values of approximately 0.6 and have bond lengths of the range 2.112–2.147 Å. Therefore, these were assigned as half OH^- and half H_2O. The ten terminal single ions all give BVS values close to 1, and both the observed bond lengths and F analysis indicate the presence of ten F^- ions. Therefore, the formula is given as $[Mn_{26}O_{17}(OH)_8(OMe)_4F_{10}(bta)_{22}(MeOH)_{14}(H_2O)_2]$, but it appears that the H^+ ions may be delocalised around the complex. While the core of **1** shows little disorder, three of the twenty-two bta^- ligands have two components, while another ten have displacement parameters that indicate the presence of disorder. Thus, the coordination environments around many of the Mn^{III} centres have an element of disorder associated with them.

The structure of $[Mn^{III}{}_{10}O_6(OH)_2(bta)_8(py)_8F_8]$ (**2**) is shown in Figure 2 (top), the crystal data are given in Table 1 and selected bond lengths and angles are given in Table 4. The core of the decametallic structure of **2** can be described as a "supertetrahedron", consisting of a tetrahedral array of Mn^{III} ions (Mn1, Mn5, Mn7 and Mn9), with Mn^{III} ions Mn2, Mn3, Mn4, Mn6, Mn8 and Mn10 capping each edge (Figure 2, middle). The Mn ions comprising the tetrahedron are each bonded to three edge-capping Mn ions through one μ_3-oxide (O1, O5, O6 and O7) and one μ_2-fluoride bridge (F5–F8). The F bridges are all asymmetric and display one short (~1.86 Å) and one long (~2.1–2.14 Å) bond, as a consequence of at least one Mn–F bond lying on a

Table 3. Bond valence sum calculations for complex **1**.

Atom	Mn^{II}	Mn^{III}	Mn^{IV}	Atom	Mn^{II}	Mn^{III}	Mn^{IV}
Mn1	3.350	3.112	3.212	Mn14	2.979	2.867	2.850
Mn2	3.291	3.055	3.133	Mn15	3.267	3.036	3.110
Mn3	3.207	2.978	3.055	Mn16	3.545	3.250	3.390
Mn4	3.277	2.994	2.893	Mn17	2.839	2.753	2.791
Mn5	3.400	3.170	3.287	Mn18	3.341	3.118	3.173
Mn6	3.423	3.162	3.093	Mn19	3.243	3.036	3.073
Mn7	3.198	2.945	3.047	Mn20	3.207	2.955	3.088
Mn8	3.293	3.072	3.128	Mn21	3.309	3.057	3.160
Mn9	3.294	3.073	3.128	Mn22	3.400	3.170	3.264
Mn10	3.479	3.300	3.433	Mn23	3.330	3.064	3.210
Mn11	3.143	2.942	3.018	Mn24	3.227	2.991	3.073
Mn12	3.305	3.072	3.149	Mn25	3.349	3.110	3.190
Mn13	3.472	3.233	3.229	Mn26	3.305	3.071	3.167

Atom	BVS	Assignment	Atom	BVS	Assignment
O3M	0.935	MeO^-	O6	0.638	OH^-/H_2O
O4M	0.889	MeO^-	O5	0.993	OH^-
O7M	0.309	MeO^-/MeOH	O23	0.631	OH^-/H_2O
O13M	0.978	MeO^-	O22	0.970	OH^-
O16M	0.920	MeO^-	O15	0.956	OH^-
O12M	0.295	MeO^-/MeOH	O12	0.988	OH^-
O1	1.944	O^{2-}	O7	1.814	O^{2-}
O2	1.771	O^{2-}	O8	1.765	O^{2-}
O3	1.817	O^{2-}	O9	1.768	O^{2-}
O4	1.810	O^{2-}	O10	1.567	O^{2-}/OH^-
O11	1.127	OH^-	O17	1.849	O^{2-}
O13	1.815	O^{2-}	O18	1.784	O^{2-}
O14	1.155	OH^-	O19	1.759	O^{2-}
O16	1.486	O^{2-}/OH^-	O20	1.825	O^{2-}
O21	1.820	O^{2-}	O25	1.833	O^{2-}
O24	1.752	O^{2-}	O26	1.920	O^{2-}
F1	0.641	F^-	F6	0.573	F^-
F2	0.569	F^-	F7	0.561	F^-
F3	0.616	F^-	F8	0.611	F^-
F4	0.617	F^-	F9	0.588	F^-
F5	0.633	F^-	F10	0.614	F^-

Jahn–Teller axis. The edge-capping metal centres are bonded to each other by a combination of μ_3-oxides and μ_3-hydroxides. The OH^- ions (O2, O3, O4 and O8) only bridge between the edge-capping centres. Each bta^- ion bridges between apex and edge-capping Mn^{III} centres in a μ_2-fashion, while each pyridine ligand bonds terminally. The coordination at each apical Mn^{III} ion is completed by a terminal fluoride ion (F1–F4). These F^- ions form hydrogen bonds to water molecules in the lattice, which in turn form hydrogen bonds to the MeOH molecules of solvation, which also form hydrogen bonds to the btaH molecule of crystallisation.

Each Mn centre displays a distorted octahedral geometry, with the expected Jahn–Teller elongations (Figure 2, bottom). The oxidation states of the Mn ions were determined by bond lengths, charge balance considerations and BVS calculations (Table 5). These clearly indicate that all the Mn ions are in the 3+ oxidation state. Identification of the inorganic bridges was also investigated by BVS analysis. Elemental analysis showed the presence of eight F^- ions, four of which bond terminally. Thus four of the remaining μ_2- or μ_3-bridges must be F^- ions. BVS calculations (Table 5) show that each μ_2-bridge has a charge of 1^-; four of the μ_3-bridges (O1, O5, O6 and O7) have a charge of 2^-, but the remaining four μ_3-bridges (O2, O3, O4 and O8) show an intermediate charge of approximately 1.5^-. To satisfy the charge balance, this leads to assignment of the μ_2-bridges as F^- ions (F5–F8), four of the μ_3-bridges as O^{2-} (O1, O5, O6 and O7) with the remaining four μ_3-bridges assigned as half OH^-, half O^{2-} (O2, O3, O4 and O8). BVS analyses suggest that O3 is almost certainly OH^-; however, because all four of these ions are related by symmetry (non-crystallographic)—each bonds in a μ_3-fashion to three of the four edge-caps—a half-O^{2-}, half OH^- description for all four is perhaps more accurate. Additional evidence for this assignment comes from the fact that each of these ions falls on the Jahn–Teller axis of a Mn^{III} ion. It is unusual for O^{2-} ions to fall on Jahn–Teller axes as these are characterised by much longer bond lengths.

The structure of the anion of $[NHEt_3]_2[Mn_3O(bta)_6(F)_3]$ (**3**) is shown in Figure 3, the crystal data are given in Table 1 and selected bond lengths and angles are given in Table 6. The $[Mn_3O(bta)_6(F)_3]^{2-}$ anion in **3** consists of three Mn^{III} centres arranged in a triangle, linked by one central μ_3-oxide (O3). Each μ_2-bta^- ligand bridges two Mn centres along one edge of the triangle. The coordination at each metal centre is completed by a terminal fluoride ion (F1–F3). The Mn^{III} ions are in Jahn–Teller distorted octahedral geometries, but the Jahn–Teller axes are not co-parallel, defined by N2-Mn1-N5, N17-Mn2-N14 and N8-Mn3-N11. The angles around the central O^{2-} range from 119.3–120.6°. Despite each edge of the triangle having the same bridges, the $\{Mn_3O\}$ unit tends towards being isosceles with the Mn3···Mn1 and Mn3···Mn2 distances being 3.260 Å in length with the Mn1···Mn2 distance slightly shorter at 3.226 Å. The MeOH solvent molecules are hydrogen-bonded to either an unbound N atom of a bta^- ligand (e.g., N18···O1, 2.737 Å) or to the cation (e.g., N20···O1, 2.695 Å).

The oxidation states of the Mn ions were determined by a combination of bond lengths (the observed Jahn–Teller elongations), charge balance considerations and bond valence sum (BVS) calculations.

Magnetic susceptibility studies: The magnetic properties of complex **1** were investigated by solid-state magnetic susceptibility (χ_M) measurements in the 5–300 K temperature range

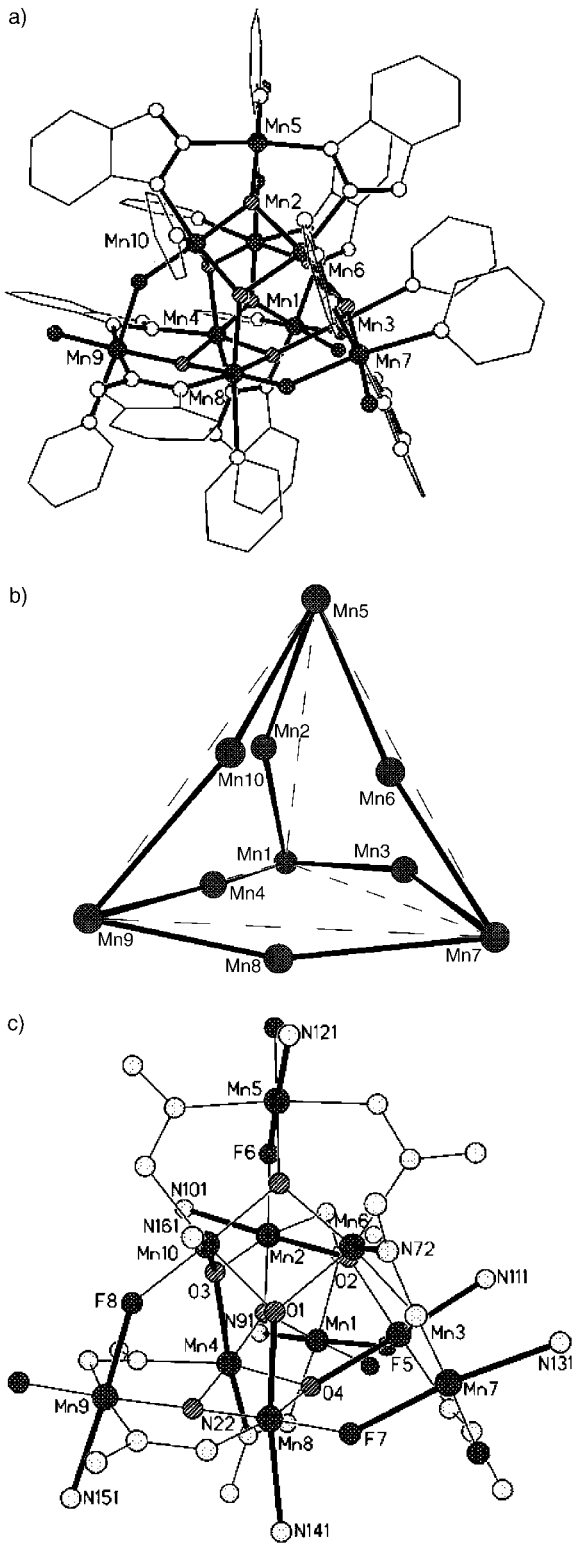

Figure 2. Top: Structure of complex **2**. Middle: The "supertetrahedral" metallic core in **2**. Bottom: Core of complex **2** showing the positions of the Jahn–Teller axes.

and in a DC field of 1 T (Figure 4, top). The room-temperature $\chi_M T$ value of approximately 55 $cm^3 K mol^{-1}$ is below that expected for 26 non-interacting Mn^{III} ions (78 $cm^3 K mol^{-1}$), which indicates the presence of strong antiferromagnetic interactions, even at 300 K. The value then drops slowly with decreasing temperature to a value of $\approx$30 $cm^3 K mol^{-1}$ at 50 K. Below 50 K, $\chi_M T$ decreases more sharply to a value of $\approx$15 $cm^3 K mol^{-1}$ at 5.0 K. This behaviour is consistent with overall antiferromagnetic exchange interactions between the Mn^{III} centres with a non-zero spin ground state, with the low-temperature value indicating an $S=4$ or 5 spin ground state.

To determine the spin ground state value for complex **1**, magnetisation measurements were carried out in the range 1.8–4 K and 0.1–0.5 T (0.1, 0.2, 0.3, 0.4 and 0.5 T, Figure 4, bottom). The data were fit by a matrix-diagonalisation method (with the program MAGNET[19]) to a model that assumes only the ground state is populated, includes axial zero-field splitting (DS_z^2) and carries out a full powder average. The best fit gave $S=4$, $g=2.0$ and $D=-0.9$ cm^{-1}. When fields up to 7 T were employed, a poorer quality fit was obtained. This behaviour is characteristic of low-lying excited states with S values greater than the ground state of $S=4$. Low-lying excited states are a common problem in large clusters,[20] and the use of only low-field data in the fits helps to avoid this problem and provides more reliable results.

The energy barrier (U) for the relaxation of magnetisation for an integer spin system with $S=4$ and $D=-0.9$ cm^{-1} is given by $S^2|D|=14.5$ cm^{-1} or 20.9 K. In order to probe whether **1** acts as an SMM, AC susceptibility measurements were performed in the 1.8–8 K temperature range in a 3.5 G AC field oscillating at 50–1000 Hz. Frequency-dependent AC susceptibility signals are seen below $\approx$3 K, but no peaks are observed (Figure 5). The magnitude of the in-phase $\chi'_M T$ versus T signals at >3 K supports a spin ground state of $S=4$. This strongly suggests that **1** exhibits SMM behaviour. To determine whether **1** is an SMM, low-temperature magnetic measurements were performed on single crystals with a micro-SQUID instrument equipped with three orthogonal field coils that allowed the applied magnetic field to be turned in all directions.[18]

Hysteresis loops were measured on a single crystal of **1** with the field applied along the easy axis of magnetisation. Below 1.2 K, hysteresis loops were observed in magnetisation versus field studies. Their coercivities increased with decreasing temperature at a sweep rate of 0.14 $T s^{-1}$ (Figure 6). The loops do not show the steplike features usually associated with quantum tunnelling of magnetisation (QTM), but appear to be typical for a cluster with a distribution of energy barriers. The steps may be present, but they broadened out owing to the inherent disorder associated with the crystal of **1**, resulting in a distribution of Mn^{III} environments. These observations have been reported for other large SMMs.[7] Relaxation data at very low temperatures were determined from DC relaxation-decay measurements (Figure 7, top). The procedure used to obtain these curves was the following: 1) a strong field was applied in order to saturate the magnetisation M to M_s and 2) the external field was suddenly set to zero. This defined the time $t=0$ s, and M was measured as a function of time. The relaxation in crystals of SMMs is often very complicated and leads to non-exponential relaxation laws. The M/M_s versus t curves of Figure 7 (top) could not be fitted by a simple law, such as

Table 4. Selected interatomic distances [Å] and angles [°] for **2**.

Mn1–O1	1.863(4)	Mn1–F1	1.814(4)	Mn1–F5	2.126(5)	Mn1–N12	2.055(7)
Mn1–N21	2.006(7)	Mn1–N91	2.248(8)	Mn2–Mn4	2.9214(15)	Mn2–O1	1.871(4)
Mn2–O2	2.165(5)	Mn2–O3	1.921(4)	Mn2–F6	1.859(3)	Mn2–N11	2.059(6)
Mn2–N101	2.245(6)	Mn3–Mn6	2.8933(14)	Mn3–O2	1.916(5)	Mn3–O4	2.152(4)
Mn3–O5	1.871(5)	Mn3–F5	1.867(4)	Mn3–N31	1.866(14)	Mn3–N31′	2.200(12)
Mn3–N111	2.274(8)	Mn4–Mn8	2.8695(17)	Mn4–O1	1.916(5)	Mn4–O3	2.087(4)
Mn4–O4	2.000(5)	Mn4–O6	1.905(5)	Mn4–N22	2.118(6)	Mn4–N42	2.079(7)
Mn5–O7	1.871(4)	Mn5–F2	1.816(4)	Mn5–F6	2.139(3)	Mn5–N51	2.021(6)
Mn5–N62	2.060(6)	Mn5–N121	2.316(13)	Mn5–N12A	2.301(8)	Mn6–Mn10	2.8874(14)
Mn6–O2	2.028(4)	Mn6–O5	1.904(5)	Mn6–O7	1.915(5)	Mn6–O8	2.046(4)
Mn6–N52	2.117(6)	Mn6–N72	2.113(6)	Mn7–O5	1.873(5)	Mn7–F3	1.813(5)
Mn7–F7	2.126(4)	Mn7–N32	2.228(17)	Mn7–N32′	1.982(11)	Mn7–N71	2.027(6)
Mn7–N131	2.257(6)	Mn8–O4	1.904(5)	Mn8–O6	1.864(5)	Mn8–O8	2.195(4)
Mn8–F7	1.862(4)	Mn8–N81	2.044(6)	Mn8–N141	2.309(7)	Mn8–N14A	2.221(12)
Mn9–O6	1.872(4)	Mn9–F4	1.801(4)	Mn9–F8	2.103(3)	Mn9–N41	2.023(7)
Mn9–N82	2.068(6)	Mn9–N151	2.261(6)	Mn10–O3	2.186(4)	Mn10–O7	1.869(4)
Mn10–O8	1.891(4)	Mn10–F8	1.856(3)	Mn10–N61	2.029(5)	Mn10–N161	2.284(5)
O1-Mn1-F1	175.1(2)	O1-Mn1-F5	88.14(18)	O1-Mn1-N12	86.5(2)	O1-Mn1-N21	88.1(2)
O1-Mn1-N91	99.2(2)	F1-Mn1-F5	87.0(2)	F1-Mn1-N12	93.3(2)	F1-Mn1-N21	92.3(2)
F1-Mn1-N91	85.6(3)	F5-Mn1-N12	87.8(2)	F5-Mn1-N21	93.7(2)	F5-Mn1-N91	171.7(2)
N12-Mn1-N21	174.3(2)	N12-Mn1-N91	88.7(3)	N21-Mn1-N91	90.5(3)	Mn4-Mn2-O1	40.09(14)
Mn4-Mn2-O2	83.29(12)	Mn4-Mn2-O3	45.48(12)	Mn4-Mn2-F6	141.06(11)	Mn4-Mn2-N11	125.87(19)
Mn4-Mn2-N101	97.16(14)	O1-Mn2-O2	94.61(19)	O1-Mn2-O3	84.46(18)	O1-Mn2-F6	177.3(2)
O1-Mn2-N11	87.7(2)	O1-Mn2-N101	90.2(2)	O2-Mn2-O3	86.25(17)	O2-Mn2-F6	88.05(17)
O2-Mn2-N11	89.8(2)	O2-Mn2-N101	172.99(17)	O3-Mn2-F6	96.23(16)	O3-Mn2-N11	170.9(2)
O3-Mn2-N101	89.10(18)	F6-Mn2-N11	91.8(2)	F6-Mn2-N101	87.24(19)	N11-Mn2-N101	95.6(2)
Mn6-Mn3-O2	44.35(14)	Mn6-Mn3-O4	84.50(11)	Mn6-Mn3-O5	40.38(15)	Mn6-Mn3-F5	139.69(17)
Mn6-Mn3-N31	133.4(4)	Mn6-Mn3-N31′	121.8(3)	Mn6-Mn3-N111	99.0(2)	O2-Mn3-O4	87.05(18)
O2-Mn3-O5	83.7(2)	O2-Mn3-F5	95.7(2)	O2-Mn3-N31	177.6(4)	O2-Mn3-N31′	165.6(4)
O2-Mn3-N111	91.4(3)	O4-Mn3-O5	95.21(19)	O4-Mn3-F5	89.00(18)	O4-Mn3-N31	93.6(3)
O4-Mn3-N31′	87.4(3)	O4-Mn3-N111	173.1(3)	O5-Mn3-F5	175.7(2)	O5-Mn3-N31	93.9(5)
O5-Mn3-N31′	83.6(4)	O5-Mn3-N111	91.3(2)	F5-Mn3-N31	86.6(5)	F5-Mn3-N31′	97.5(4)
F5-Mn3-N111	84.5(2)	N31-Mn3-N31′	12.6(5)	N31-Mn3-N111	88.3(4)	N31′-Mn3-N111	95.6(3)
Mn2-Mn4-Mn8	114.98(4)	Mn2-Mn4-O1	38.97(12)	Mn2-Mn4-O3	41.03(11)	Mn2-Mn4-O4	93.47(14)
Mn2-Mn4-O6	133.88(13)	Mn2-Mn4-N22	122.63(19)	Mn2-Mn4-N42	101.09(18)	Mn8-Mn4-O1	136.77(15)
Mn8-Mn4-O3	92.31(12)	Mn8-Mn4-O4	41.40(14)	Mn8-Mn4-O6	39.90(13)	Mn8-Mn4-N22	102.9(2)
Mn8-Mn4-N42	123.49(19)	O1-Mn4-O3	78.98(17)	O1-Mn4-O4	97.6(2)	O1-Mn4-O6	172.73(18)
O1-Mn4-N22	84.0(2)	O1-Mn4-N42	98.6(2)	O3-Mn4-O4	98.47(17)	O3-Mn4-O6	94.28(17)
O3-Mn4-N22	162.5(2)	O3-Mn4-N42	87.67(19)	O4-Mn4-O6	80.56(19)	O4-Mn4-N22	87.6(2)
O4-Mn4-N42	163.5(2)	O6-Mn4-N22	102.9(2)	O6-Mn4-N42	83.7(2)	N22-Mn4-N42	91.0(2)
O7-Mn5-F2	176.25(17)	O7-Mn5-F6	89.00(16)	O7-Mn5-N51	87.5(2)	O7-Mn5-N62	86.48(19)
O7-Mn5-N121	92.1(3)	O7-Mn5-N12A	99.5(2)	F2-Mn5-F6	87.26(16)	F2-Mn5-N51	92.6(2)
F2-Mn5-N62	93.3(2)	F2-Mn5-N121	91.7(3)	F2-Mn5-N12A	84.2(2)	F6-Mn5-N51	92.78(19)
F6-Mn5-N62	86.23(16)	F6-Mn5-N121	178.4(3)	F6-Mn5-N12A	167.2(2)	N51-Mn5-N62	174.0(2)
N51-Mn5-N121	86.1(4)	N51-Mn5-N12A	97.2(2)	N62-Mn5-N121	95.0(4)	N62-Mn5-N12A	84.7(2)
N121-Mn5-N12A	13.1(3)	Mn3-Mn6-Mn10	114.66(4)	Mn3-Mn6-O2	41.33(14)	Mn3-Mn6-O5	39.54(15)
Mn3-Mn6-O7	136.90(13)	Mn3-Mn6-O8	91.85(11)	Mn3-Mn6-N52	102.80(17)	Mn3-Mn6-N72	122.70(17)
Mn10-Mn6-O2	93.91(13)	Mn10-Mn6-O5	134.05(14)	Mn10-Mn6-O7	39.67(12)	Mn10-Mn6-O8	40.76(12)
Mn10-Mn6-N52	122.72(18)	Mn10-Mn6-N72	101.79(17)	O2-Mn6-O5	79.9(2)	O2-Mn6-O7	97.90(19)
O2-Mn6-O8	98.58(17)	O2-Mn6-N52	86.7(2)	O2-Mn6-N72	162.3(2)	O5-Mn6-O7	173.48(18)
O5-Mn6-O8	94.74(18)	O5-Mn6-N52	102.5(2)	O5-Mn6-N72	83.3(2)	O7-Mn6-O8	79.46(17)
O7-Mn6-N52	83.4(2)	O7-Mn6-N72	99.4(2)	O8-Mn6-N52	162.6(2)	O8-Mn6-N72	88.3(2)
N52-Mn6-N72	91.5(2)	O5-Mn7-F3	178.3(2)	O5-Mn7-F7	90.22(19)	O5-Mn7-N32	79.5(5)
O5-Mn7-N32′	91.7(4)	O5-Mn7-N71	87.4(2)	O5-Mn7-N131	94.8(2)	F3-Mn7-F7	88.09(19)
F3-Mn7-N32	100.4(5)	F3-Mn7-N32′	88.1(4)	F3-Mn7-N71	92.8(2)	F3-Mn7-N131	86.8(2)
F7-Mn7-N32	87.0(3)	F7-Mn7-N32′	85.9(2)	F7-Mn7-N71	92.9(2)	F7-Mn7-N131	172.7(2)
N32-Mn7-N32′	12.3(5)	N32-Mn7-N71	166.9(5)	N32-Mn7-N131	88.6(3)	N32′-Mn7-N71	178.5(3)
N32′-Mn7-N131	88.6(3)	N71-Mn7-N131	92.6(2)	Mn4-Mn8-O4	44.02(14)	Mn4-Mn8-O6	40.96(14)
Mn4-Mn8-O8	84.18(12)	Mn4-Mn8-F7	140.67(14)	Mn4-Mn8-N81	126.49(18)	Mn4-Mn8-N141	104.46(19)
Mn4-Mn8-N14A	91.5(3)	O4-Mn8-O6	84.2(2)	O4-Mn8-O8	84.95(17)	O4-Mn8-F7	97.2(2)
O4-Mn8-N81	170.4(2)	O4-Mn8-N141	97.2(2)	O4-Mn8-N14A	86.1(4)	O6-Mn8-O8	95.52(18)
O6-Mn8-F7	177.8(2)	O6-Mn8-N81	86.7(2)	O6-Mn8-N141	94.8(2)	O6-Mn8-N14A	86.6(3)
O8-Mn8-F7	86.38(16)	O8-Mn8-N81	93.1(2)	O8-Mn8-N141	169.6(2)	O8-Mn8-N14A	170.6(3)
F7-Mn8-N81	92.1(2)	F7-Mn8-N141	83.3(2)	F7-Mn8-N14A	91.7(3)	N81-Mn8-N141	86.4(3)
N81-Mn8-N14A	96.2(4)	N141-Mn8-N14A	13.2(4)	O6-Mn9-F4	176.98(19)	O6-Mn9-F8	89.94(16)
O6-Mn9-N41	87.3(2)	O6-Mn9-N82	85.4(2)	O6-Mn9-N151	94.7(2)	F4-Mn9-F8	87.18(16)
F4-Mn9-N41	93.9(2)	F4-Mn9-N82	93.5(2)	F4-Mn9-N151	88.1(2)	F8-Mn9-N41	95.48(19)
F8-Mn9-N82	84.79(19)	F8-Mn9-N151	172.7(2)	N41-Mn9-N82	172.6(2)	N41-Mn9-N151	90.4(2)

Table 4. (Continued)

N82-Mn9-N151	89.9(2)	Mn6-Mn10-O3	83.44(11)	Mn6-Mn10-O7	40.87(14)	Mn6-Mn10-O8	44.95(13)
Mn6-Mn10-F8	140.99(12)	Mn6-Mn10-N61	127.24(15)	Mn6-Mn10-N161	98.06(13)	O3-Mn10-O7	95.71(16)
O3-Mn10-O8	85.12(17)	O3-Mn10-F8	86.50(15)	O3-Mn10-N61	91.59(18)	O3-Mn10-N161	168.04(18)
O7-Mn10-O8	84.76(19)	O7-Mn10-F8	177.44(17)	O7-Mn10-N61	88.1(2)	O7-Mn10-N161	93.06(18)
O8-Mn10-F8	96.74(17)	O8-Mn10-N61	171.8(2)	O8-Mn10-N161	87.61(19)	F8-Mn10-N61	90.54(18)
F8-Mn10-N161	84.94(17)	N61-Mn10-N161	96.81(19)				
Mn1-O1-Mn2	125.5(2)	Mn1-O1-Mn4	124.7(3)	Mn2-O1-Mn4	100.93(19)	Mn2-O2-Mn3	128.0(2)
Mn2-O2-Mn6	124.2(2)	Mn3-O2-Mn6	94.3(2)	Mn2-O3-Mn4	93.48(16)	Mn2-O3-Mn10	127.71(19)
Mn4-O3-Mn10	125.1(2)	Mn3-O4-Mn4	124.3(3)	Mn3-O4-Mn8	129.3(2)	Mn4-O4-Mn8	94.58(19)
Mn3-O5-Mn6	100.1(2)	Mn3-O5-Mn7	124.9(2)	Mn6-O5-Mn7	125.5(3)	Mn4-O6-Mn8	99.14(19)
Mn4-O6-Mn9	124.6(3)	Mn8-O6-Mn9	126.3(2)	Mn5-O7-Mn6	125.1(2)	Mn5-O7-Mn10	125.1(2)
Mn6-O7-Mn10	99.5(2)	Mn6-O8-Mn8	125.8(2)	Mn6-O8-Mn10	94.28(19)	Mn8-O8-Mn10	128.0(2)
Mn1-F5-Mn3	138.4(2)	Mn2-F6-Mn5	139.0(2)	Mn7-F7-Mn8	137.5(2)	Mn9-F8-Mn101	39.1518

Table 5. Bond valence sum calculations for complex **2**.

Atom	Mn^{II}	Mn^{III}	Mn^{IV}	Atom	Mn^{II}	Mn^{III}	Mn^{IV}
Mn1	3.330	3.153	3.263	Mn6	3.288	3.058	3.127
Mn2	3.307	3.062	3.192	Mn7	3.278	3.058	3.174
Mn3	3.392	3.145	3.267	Mn8	3.327	3.052	3.181
Mn4	3.319	3.283	3.155	Mn9	3.352	3.062	3.247
Mn5	3.269	3.052	3.162	Mn10	3.367	3.118	3.249

Atom	BVS	Assignment	Atom	BVS	Assignment
O1	2.072	O^{2-}	O5	2.073	O^{2-}
O2	1.406	O^{2-}/OH^{-}	O6	2.089	O^{2-}
O3	1.259	O^{2-}/OH^{-}	O7	2.062	O^{2-}
O4	1.475	O^{2-}/OH^{-}	O8	1.408	OH^{-}/O^{2-}
F5	0.986	F^{-}	F7	0.996	F^{-}
F6	0.991	F^{-}	F8	1.028	F^{-}

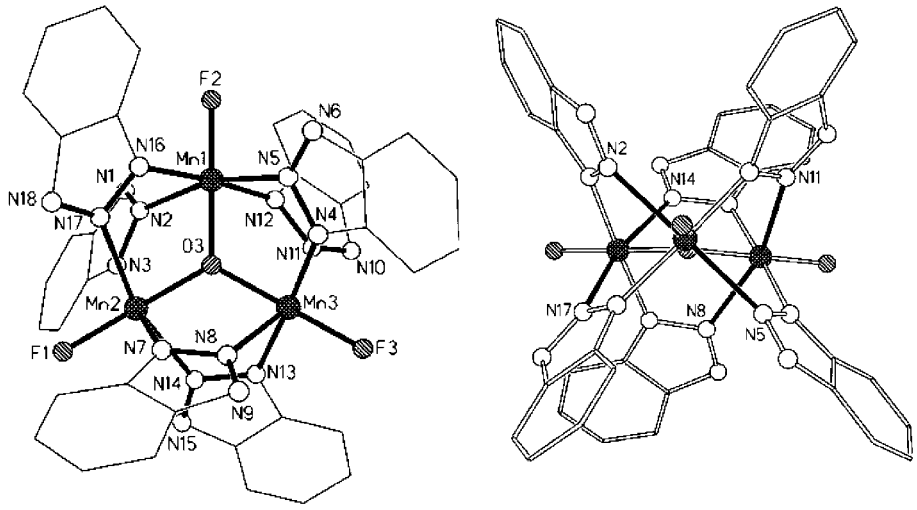

Figure 3. Left: Structure of complex **3**. Right: Side view indicating the positions of the Jahn–Teller axes.

exponential, stretched exponential, square root, and so forth. To extract the temperature dependence of the mean relaxation time $\tau(T)$, we used a single scaling function $f(t/\tau(T))$.[21] The master function $f(x)$ is such that $f(t=0)=M$ and $f(t=\infty)=0$. All the data points of the relaxation measurements between 0.04 and 1.2 K and between $t=2$ and 1000 s are scaled on a single master curve using the transformation $t/\tau(T)$. This leads to the scaling plot of $M(t)$ versus $t/\tau(T)$ shown in Figure 7 (bottom). This scaling analysis allows $\tau(T)$ to be determined without making any particular assumption about the relaxation law, and allows the mean relaxation time $\tau(T)$ to be extracted. A fit of these data to the Arrhenius Law [Eq. (1), Figure 8] gave an effective mean barrier for the reversal of magnetisation of approximately 15 K and a pre-exponential factor of $\tau_0=3\times10^{-9}$ s.

$$\tau = \tau_o \exp(U_{eff}/kT) \qquad (1)$$

Below ~0.2 K, the relaxation rates become independent of temperature, which strongly suggests the presence of QTM in the ground state. The experimentally derived U_{eff} value of 15 K is comparable to the theoretical value ($U=20.9$ K). Indeed, U is expected to be larger than U_{eff} because the reversal of magnetisation has two components: 1) thermally activated relaxation over the barrier and 2) quantum tunnelling of magnetisation (QTM) through the barrier.

The magnetic properties of complex **2** were investigated by solid-state magnetic susceptibility (χ_M) measurements in the 5–300 K temperature range in a DC field of 1 T. (Figure 9). The room temperature $\chi_M T$ value of ~21 $cm^3 K mol^{-1}$ K, which is below that expected for ten noninteracting $S=2$ centres (~30 $cm^3 K mol^{-1}$), drops slowly to a value of 12 $cm^3 K mol^{-1}$ at 50 K, and then decreases more rapidly to 5.4 $cm^3 K mol^{-1}$ at 5 K. These data

Table 6. Interatomic distances [Å] and angles [°] for **3**.

F1–Mn2	1.8108(14)	F2–Mn1	1.8072(14)	F3–Mn3	1.8049(14)	Mn1–O3	1.8741(17)
Mn1–N12	1.996(2)	Mn1–N16	2.022(2)	Mn1–N5	2.305(2)	Mn1–N2	2.334(2)
Mn1–Mn2	3.2259(6)	Mn2–O3	1.8635(16)	Mn2–N7	2.003(2)	Mn2–N3	2.024(2)
Mn2–N14	2.295(2)	Mn2–N17	2.372(2)	Mn3–O3	1.8894(16)	Mn3–N13	2.011(2)
Mn3–N4	2.012(2)	Mn3–N11	2.317(2)	Mn3–N8	2.362(2)		
F2-Mn1-O3	178.80(7)	F2-Mn1-N12	92.43(8)	O3-Mn1-N12	86.72(8)	F2-Mn1-N16	91.83(8)
O3-Mn1-N16	88.98(8)	N12-Mn1-N16	175.07(8)	F2-Mn1-N5	99.13(7)	O3-Mn1-N5	81.73(7)
N12-Mn1-N5	89.94(8)	N16-Mn1-N5	91.83(8)	F2-Mn1-N2	96.46(7)	O3-Mn1-N2	82.68(7)
N12-Mn1-N2	89.24(8)	N16-Mn1-N2	87.82(8)	N5-Mn1-N2	164.41(8)	F2-Mn1-Mn2	149.63(5)
O3-Mn1-Mn2	30.24(5)	N12-Mn1-Mn2	105.83(6)	N16-Mn1-Mn2	69.26(6)	N5-Mn1-Mn2	104.83(5)
N2-Mn1-Mn2	60.56(5)	F1-Mn2-O3	179.39(7)	F1-Mn2-N7	92.75(8)	O3-Mn2-N7	87.00(8)
F1-Mn2-N3	91.45(8)	O3-Mn2-N3	88.81(8)	N7-Mn2-N3	175.59(8)	F1-Mn2-N14	96.76(7)
O3-Mn2-N14	82.68(7)	N7-Mn2-N14	88.11(8)	N3-Mn2-N14	92.73(8)	F1-Mn2-N17	98.95(7)
O3-Mn2-N17	81.60(7)	N7-Mn2-N17	88.89(8)	N3-Mn2-N17	89.13(8)	N14-Mn2-N17	164.12(8)
F1-Mn2-Mn1	150.15(5)	O3-Mn2-Mn1	30.43(5)	N7-Mn2-Mn1	107.12(6)	N3-Mn2-Mn1	68.49(6)
N14-Mn2-Mn1	105.74(5)	N17-Mn2-Mn1	60.44(5)	F3-Mn3-O3	179.89(8)	F3-Mn3-N13	91.43(8)
O3-Mn3-N13	88.67(8)	F3-Mn3-N4	91.61(8)	O3-Mn3-N4	88.29(8)	N13-Mn3-N4	176.90(8)
F3-Mn3-N11	99.67(8)	O3-Mn3-N11	80.35(8)	N13-Mn3-N11	92.09(8)	N4-Mn3-N11	88.00(8)
F3-Mn3-N8	100.18(8)	O3-Mn3-N8	79.80(8)	N13-Mn3-N8	87.26(8)	N4-Mn3-N8	91.60(8)
N11-Mn3-N8	160.15(7)	Mn2-O3-Mn1	119.33(8)	Mn2-O3-Mn3	120.59(9)	Mn1-O3-Mn3	120.07(9)

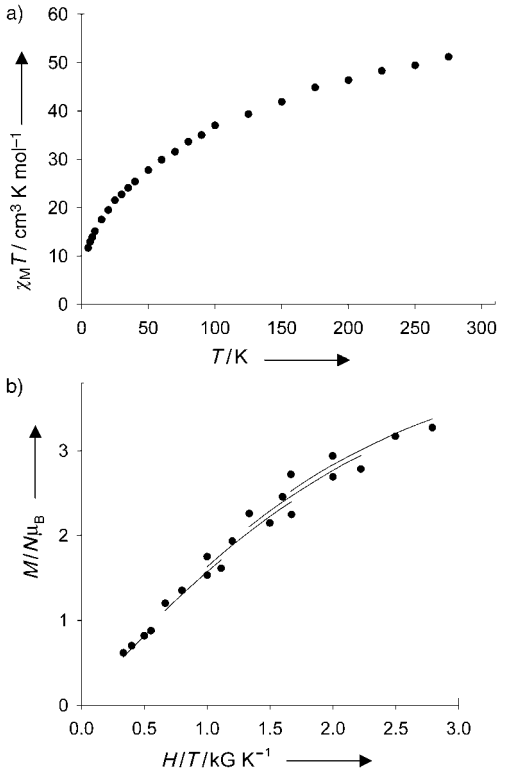

Figure 4. Top: Magnetic susceptibility data for **1**, plotted as $\chi_M T$ versus T. Bottom: Magnetisation data for **1**, plotted as reduced magnetisation (M/N_{μ_B}) versus H/T.

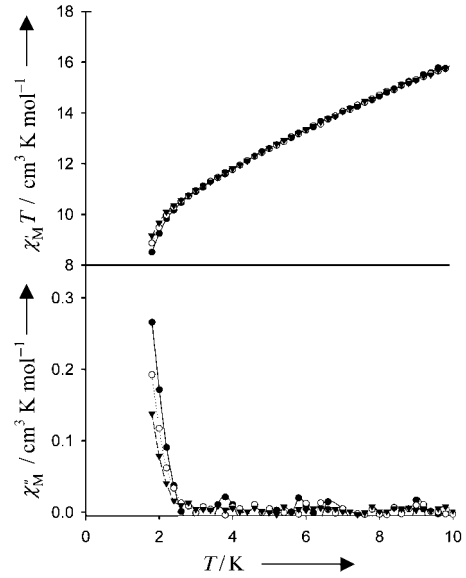

Figure 5. Plots of the in-phase (χ'_M) signal as $\chi'_M T$ and out-of-phase (χ''_M) signal in AC susceptibility studies versus T for complex **1**.

strongly indicate antiferromagnetic exchange interactions between the Mn^{III} ions, leading to a small spin ground spin state, possibly $S=0$. To determine the value of the spin ground state, magnetisation measurements were carried out at 1.8–4 K and 0.1–7 T. Attempts to fit the data (using the same procedure as above) resulted in poor quality and unreliable fits (Figure S1 in the Supporting Information). This is probably attributable to the presence of low-lying excited states, which are a common problem with large cluster aggregates. In this case, they may result from the presence of bridging fluorides that are expected to promote weak exchange interactions between the metal centres. Variable-temperature AC susceptibility experiments were performed over the temperature range of 1.8–8 K at frequencies of 50–1000 Hz, with zero applied DC magnetic field and a 3.5 G oscillating AC magnetic field. Extrapolation of the in-phase susceptibility plot suggests a low ground-spin state close to zero (Figure S2 in the Supporting Information). In addition, no frequency-dependent AC signals are seen. The above data suggest complex **2** probably possesses an $S=0$ spin ground state with low-lying excited states.

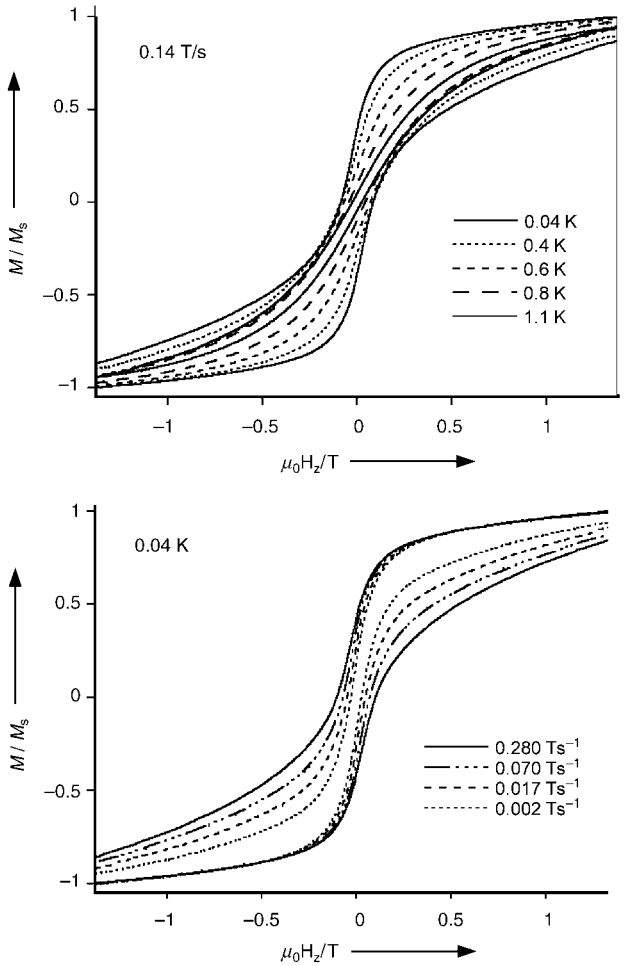

Figure 6. Magnetisation (M) of **1** (plotted as a fraction of the maximum value M_s) versus applied magnetic field ($\mu_0 H_z$). The resulting hysteresis loops are shown at different temperatures (top) and different field sweep rates (bottom).

Solid-state DC magnetic susceptibility studies were performed on **3** in the 5–300 K temperature range in a field of 1 T. The room temperature $\chi_M T$ value of approximately 8.8 $cm^3 K mol^{-1}$ (which is consistent with the spin-only value for three noninteracting Mn^{III} ions; ~9 $cm^3 K mol^{-1}$) drops slowly with temperature, reaching a $\chi_M T$ value of ~8 $cm^3 K mol^{-1}$ at 125 K, before falling more sharply to a value of ~2 $cm^3 K mol^{-1}$ at 5 K (Figure 10, top). These data suggest dominant antiferromagnetic exchange interactions between the Mn^{III} metal centres with a small spin ground state. Complex **3** can be regarded as either an equilateral or isosceles triangle, because there is only a small "distortion" present in the triangle topology. Attempts to fit the data to a one J model proved unsatisfactory, and a better replication of the experimental data was found with a two J model that employed the spin Hamiltonian shown in Equation (2), in which J_a represents the Mn3–Mn1 and Mn3–Mn2 (3.260(6) Å) exchange interaction parameter, and J_b represents the Mn2–Mn1 (3.226(6) Å) exchange interaction (Scheme 1).

$$\hat{\boldsymbol{H}} = -2[J_a(\hat{\boldsymbol{S}}_3\hat{\boldsymbol{S}}_2) + J_a(\hat{\boldsymbol{S}}_3\hat{\boldsymbol{S}}_1) + J_b(\hat{\boldsymbol{S}}_2\hat{\boldsymbol{S}}_1)] \quad (2)$$

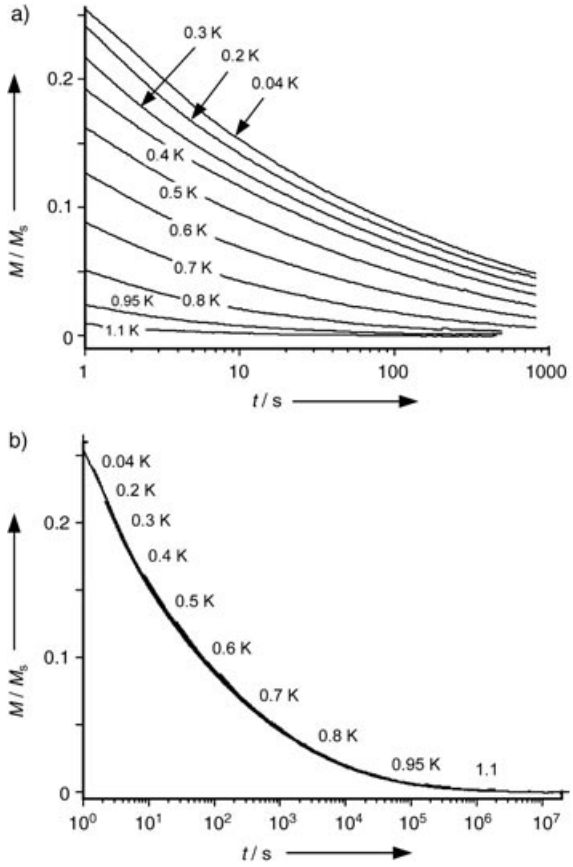

Figure 7. Top: Relaxation data for **1**, plotted as fraction of maximum value M_s versus time. Bottom: Scaling of the relaxation of **1** to a master curve.

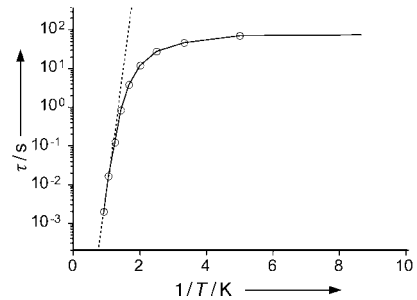

Figure 8. Arrhenius plot of **1** from DC decay data on a single crystal. Fit of the data in the thermally activated region (——) and fit of the temperature-independent data (-----).

The fit at high temperature (>20 K) to the experimental $\chi_M T$ data (Figure 10, top) suggests a ground state spin of $S=2$ with the following parameters: $g=2.00$ and $J_a=-5.01$ cm^{-1}, $J_b=+9.16$ cm^{-1}. Thus, the ground state spin $S=2$ could be rationalised by considering two "spin-up" and one "spin-down" Mn^{III} centres. The first excited state ($S=3$) was predicted to be 30.1 cm^{-1} above the ground state. Attempts to fit the data with different parameters (which included generating an $S=1$ ground state with this model, see below) resulted in much poorer fits.

In order to identify the ground state, magnetisation measurements (M) were then carried out in the temperature

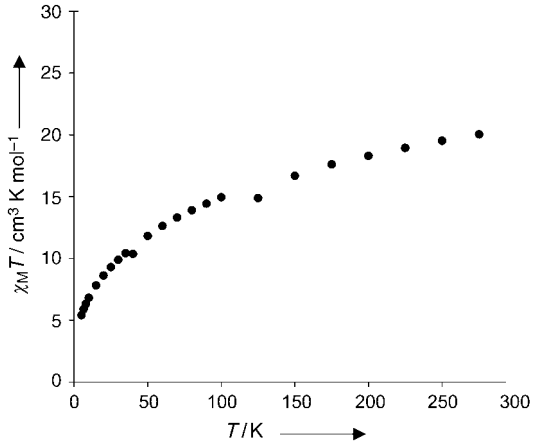

Figure 9. Variable-temperature magnetic susceptibility data for **2**, plotted as $\chi_M T$ versus T.

range 1.8–4.0 K in nine different external magnetic fields of 0.1, 0.5, 1.0, 2.0, 3.0, 4.0, 5.0, 6.0 and 7.0 T (Figure 10, bottom). Although the data at the highest field and lowest temperatures saturates at a M/N_{μ_B} value of 3.2—only slightly lower than the expected value of 4.0 for an $S=2$ ground state with $g=2.0$—no satisfactory fit of the data could be obtained. Clearly the presence of low-lying excited states is responsible for this problem and as such no definite value for the spin ground state can be obtained from the DC measurements alone. Therefore, AC susceptibility experiments were performed over the temperature range of 1.8–8 K at frequencies of 50–1000 Hz, with zero applied DC magnetic field and a 3.5 G oscillating AC magnetic field. Extrapolation of the in-phase susceptibility ($\chi_M'T$) plot suggests a low ground-spin state, but one that is more consistent with an $S=1$ ground state rather than an $S=2$ ground state (Figure S3 in the Supporting Information). The AC and DC data thus confirm the presence of low-lying excited states and hence the difficulty in fitting the DC data. The fitting above [that used the Hamiltonian in Eq. (2)] suggests a ferromagnetic exchange between Mn1 and Mn2. This result is somewhat surprising, firstly, given that the two ions are bridged by an O^{2-} ion at an angle of approximately 119° and secondly, because previous studies of $\{Mn_3O\}$ units have indicated weak antiferromagnetic exchange,[22] although weak ferromagnetic exchange has been observed in mono-oxo bridged Mn^{III}–Mn^{III} dimers.[23] Indeed, given the topology we would expect complex **3** to be subject to some degree of spin frustration. In order to address this problem, to identify the spin ground state and to gain more detailed understanding of the exchange interactions involved in **3**, DFT calculations were performed.

Noodleman's broken symmetry approach has been widely used to evaluate exchange interactions in metal complexes[24] and a combination of the B3LYP functional with Ahlrich's basis set has been shown to yield good numerical estimates of exchange interactions.[25a,b] Recently, the evaluation of exchange interactions in polynuclear metal complexes has been formulated and tested on several benchmark systems.[26] Here, we have performed density functional calculations on the anion of **3**, $[Mn_3O(bta)_6F_3]^{2-}$, (in

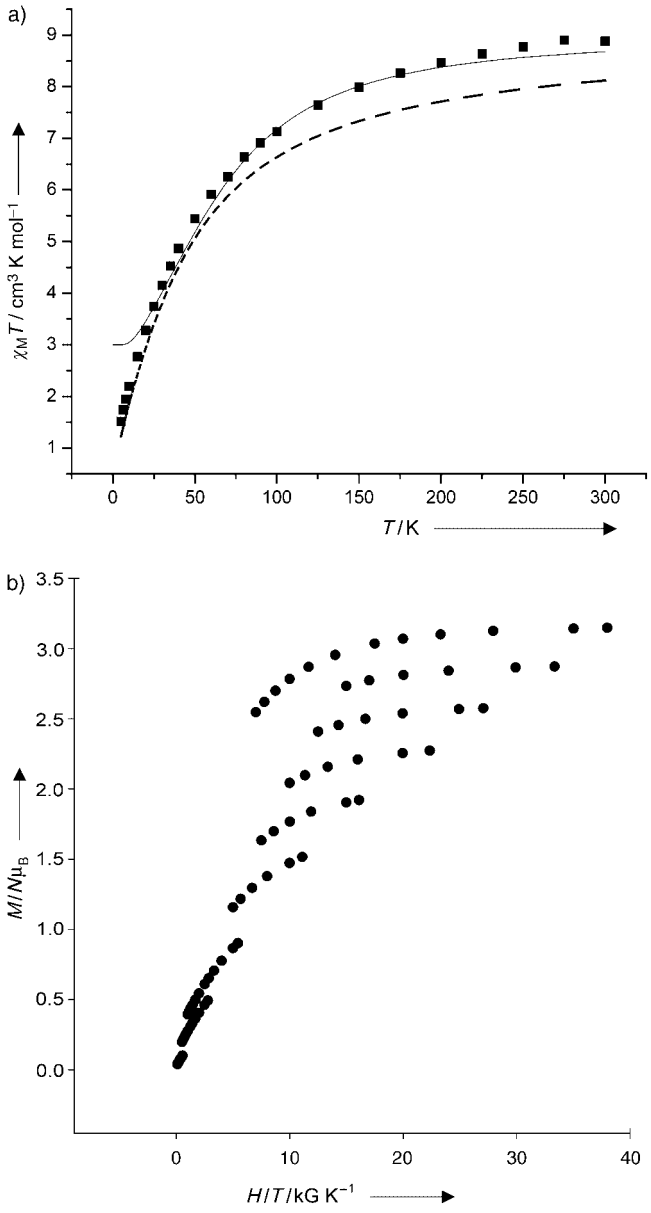

Figure 10. Top: Variable-temperature magnetic susceptibility data for **3** plotted as $\chi_M T$ versus T; (■) experimental; (——) experimental fit; (-----) DFT fit. Bottom: Magnetisation data for **3**, plotted as reduced magnetisation (M/N_{μ_B}) versus H/T.

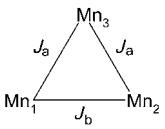

Scheme 1. The exchange interactions present in **3**.

which the counterions have been removed from the crystal structure to reduce computational time) in order to calculate the exchange interactions between the neighbouring metal centres. The calculations were performed with the GAUSSIAN98 suite of programs.[27] Ahlrich's triple-zeta basis set was used for the metal atoms and a double-zeta basis set on the non-metals. To avoid convergence problems,

Jaguar 5.0 was used to generate the initial guess, and this was then transferred to Gaussian to proceed further. Considering the degree of accuracy needed for the evaluation of energies of the spin configurations, single-point calculations were performed with tight convergence criteria. In the present case, the experimental fitting was carried out with two non-equivalent exchange interactions ($J_a = -5.01\ cm^{-1}$ and $J_b = +9.16\ cm^{-1}$), and so the DFT calculations have been performed assuming the same exchange topology. The energy differences between the calculated spin configurations can be related to the exchange interactions by a pairwise interaction model.[28] The spin configurations (ST1–ST3) used to calculate the energies are shown in Figure 11. The relationship between the exchange interactions and the energy difference is given in Equations (3) and (4):

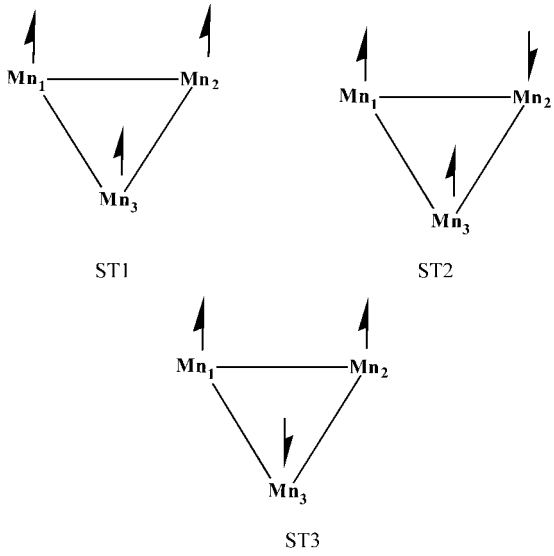

Figure 11. The spin configurations (ST1, ST2, ST3) chosen to calculate the exchange interactions.

$$\frac{E_{ST1} - E_{ST2}}{2S_1S_2 + S_2} = -2J_a - 2J_b \quad (3)$$

$$\frac{E_{ST1} - E_{ST3}}{2S_1S_2 + S_2} = -4J_a \quad (4)$$

In these equations S_1 and S_2 are the spins on the metal centres, in this case $S_1 = S_2 = 2$. Calculations yield $J_a = -2.95\ cm^{-1}$ and $J_b = -2.12\ cm^{-1}$. This suggests that both interactions are weakly antiferromagnetic, in contrast to the experimental values in which J_b is ferromagnetic. A comparison of the experimental curve with the DFT calculated values (Figure 10, top) gives a poorer fit in the high-temperature region, but a better fit in the low-temperature region. However, it is important to note that the theoretical calculations do not take account of the anisotropy arising from the presence of Mn^{III} ions, which is likely to be important at lower temperatures, especially given that the exchange interactions are small. The DFT calculated values give a ground state of $S = 0$ with two $S = 1$ states at $1.46\ cm^{-1}$ and $5.9\ cm^{-1}$, and an $S = 2$ state at $6.1\ cm^{-1}$ above the ground state. This helps to explain our inability to obtain a satisfactory fit of the DC magnetisation data. The ground state of this molecule can be changed from 0 to 2 by introducing small changes in the exchange interaction J_b. The ratio of J_a/J_b versus the Eigen values obtained for these exchange parameters is shown in Figure 12. For a value of $J_a/J_b < 1$, the

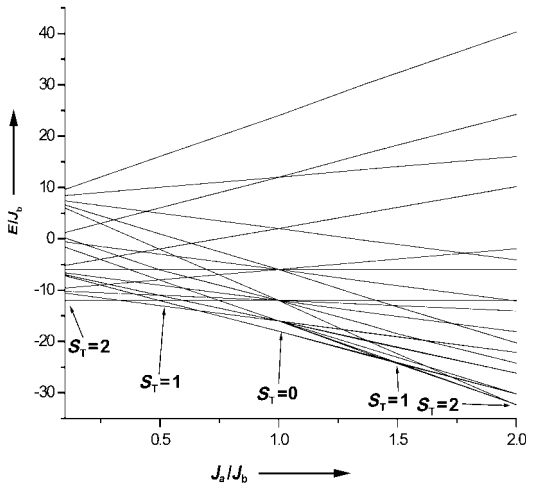

Figure 12. Plot of calculated eigen values versus J_a/J_b for **3**.

ground state spin value varies from $S = 2$ to $S = 1$, for $J_a/J_b = 1$ the ground state becomes $S = 0$ and for $J_a/J_b > 1$ the ground state varies from $S = 0$ to $S = 2$. For the DFT calculated values, the J_a/J_b ratio is found to be 1.37 and the ground state is $S = 0$. However, it is also clear from Figure 12 that the energy levels are very closely separated for $J_a/J_b > 1$, and the fact that the ground state depends on the ratio of J_a/J_b reveals that a degree of spin frustration exists in the triangle. At lower and higher values of J_a/J_b the degree of spin frustration is minimal, giving rise to an $S = 2$ ground state that can be accounted for by a simple pairwise exchange interaction. At intermediate values of J_a/J_b, spin frustration causes a net spin vector alignment, which cannot be accounted for by considering a simple pairwise exchange interaction, and the value of the ground state depends on the degree of spin frustration. This kind of behaviour has been observed in mixed valence ($2 \times Mn^{III}$, $1 \times Mn^{II}$) manganese triangles.[28]

DFT-calculated spin densities can serve as a basis for understanding the nature of magnetic interactions and can be used to explain the mechanism of the exchange operating in a molecule.[29,25b] The DFT-computed spin densities for the ST1 and ST2 configurations are shown in Table 7 and the plotted spin density for the high spin state (ST1) is given in Figure 13. The modulus of the spin densities on each manganese atom is calculated to be >3.8 for both configurations, indicating that the magnetic orbitals are centred on the metals and that there is some unpaired spin density on the ligands.

Starting at the atom with the highest unpaired spin density (Mn in this case), a spin polarisation mechanism will result in spin density of opposite sign in atoms bonded di-

Table 7. DFT-computed spin densities on atoms for configurations ST1 and ST2.

Atom	ST1	ST2
Mn1	3.836	3.812
Mn2	3.837	−3.793
Mn3	3.845	3.821
O3	0.013	0.001
F2	0.066	0.061
F1	0.065	−0.057
F2	0.064	0.060
N4	−0.035	−0.037
N5	0.046	0.046
N11	0.050	0.050
N12	−0.035	−0.036
N8	0.047	0.035
N7	−0.034	0.034
N13	−0.035	−0.034
N14	0.048	−0.037
N3	−0.033	−0.032
N2	0.043	−0.033
N17	0.046	0.035
N16	−0.033	0.034
N18	0.016	−0.016
C31	0.001	0.007
C36	0.003	−0.004
C35	−0.002	0.002
C34	0.006	−0.005
C33	−0.004	0.004
C32	0.012	−0.008

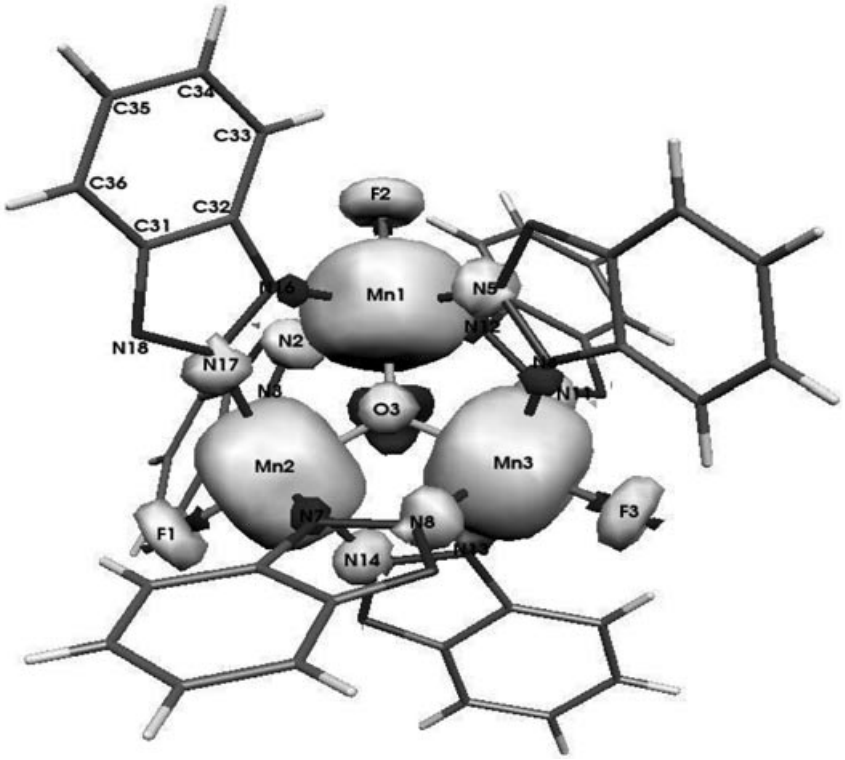

Figure 13. DFT-calculated spin density distribution for the spin configuration ST1.

rectly to it and the same sign for atoms that are two bonds away. This alternation in sign is continued through the bonds and attenuates with the distance from the primary source of the unpaired spin density. In a spin delocalisation mechanism, spin density of the same sign is generated on the directly bonded atom, as well as on atoms that are two or more bonds away, and attenuates with distance from the primary source of the unpaired spin density. The net spin density (given in Table 7) at a particular atom is the sum of the spin densities of each atomic orbital of that atom. The net spin density results from the combination of the two mechanisms and the sign of the net spin density is determined by the predominant mechanism (for a directly bonded atom, a positive spin on the "source" atom will give positive if spin delocalisation predominates and negative if spin polarisation predominates). In Figure 13, a net spin density that arises from a pure delocalisation mechanism is represented in white, and a pure polarisation mechanism is represented in black. If both mechanisms are operating on a particular atom, this can be observed as a combination of both colours.

The terminal fluoride ions have the same sign of the spin density as the Mn atoms to which they are bound in both ST1 and ST2; this indicates that the spin delocalisation mechanism dominates. The total spin density on the μ_3-oxygen atom is 0.013 for ST1 and 0.001 for ST2. This suggests that the mechanisms of spin polarisation and delocalisation are competing here, as can be seen in Figure 13, noting also that the spin densities on the remote carbon atoms of the benzotriazolate rings are in the range 0.001–0.012. In general, spin delocalisation attenuates with distance from the metal centre. At a "two-atom" distance from the metal centre spin alternation appears (e.g., C33, C34, C35, C36), and this reveals that spin polarisation is the predominant mechanism here.

There are two kinds of spin density distribution observed for the bridging nitrogen atoms: a positive spin density is found along one metal axis (e.g., N2-Mn1-N5), with a negative spin density on the other axis (e.g., N16-Mn1-N12). The positive and the negative spin densities arise from spin delocalisation and spin polarisation mechanisms, respectively. Thus, spin delocalisation is observed to dominate on the Jahn–Teller axes of the Mn^{III} ions.

Considering that spin density distribution in a molecule with unpaired electrons results from these two mechanisms, if the unpaired spin density is in the metal π orbital (e.g., t_{2g}), spin density on the ligands may be negative due to spin polarisation—if spin delocalisation is very small. This is true for most electronegative atoms, such as F and O. If the unpaired spin density is on

the metal σ orbital (e.g., e_g), spin delocalisation is always the predominant mechanism. In the present case, unpaired spin density is found on both the π and σ orbitals and, hence, a competition between the two mechanisms occurs on the most electronegative atoms, such as F and O. In the case of the N atom, spin delocalisation predominates on the σ orbital (Jahn–Teller) axis and spin polarisation dominates on the others.

The spin density distribution can be used to predict the nature of interactions in metal clusters, although it is complicated because both mechanisms operate; however, the sign of the spin density is determined by the dominant mechanism. This result shows that, in the case of a Jahn–Teller distorted octahedral Mn^{III} ion, the elongated axis will favour a spin delocalisation mechanism.

Conclusion

This work shows that MnF_3 is an excellent precursor for the synthesis of high nuclearity Mn^{III} clusters. It provides a source of Mn^{III} without the need for oxidising Mn^{II} species or the use of the triangular $[Mn_3O(O_2CR)_6(L)_3]^{0/+}$ species. Complexes **1**–**3** were all made from similar reactions, whereby the identity of the cluster isolated is controlled by the nature of the base added. Complex **1** is the first polymetallic cage to be synthesised from MnF_3, achieved by the simple reaction between MnF_3 and btaH in hot MeOH. It is a rare example of a Mn^{III} cluster predominantly composed of nitrogen-based bridging ligands. Complex **1** is the third largest Mn cluster, and the third largest cluster to exhibit SMM behaviour. Complex **2** is a rare example of a cluster with a "supertetrahedral" metal core, and possesses an $S=0$ spin ground state. Complex **3** is a rare example of an oxo-centred trimetallic cluster in which the M^{III} centres are bridged by ligands other than carboxylates and in which the terminal ligands are fluorides. Its magnetic behaviour suggests an $S=0$ or $S=1$ spin ground state with a low-lying $S=2$ excited state. The synthesis of **1**–**3** suggests that the addition of different bases and counterions might lead to even more products, and, given the success $[Mn_3O(O_2CR)_6(L)_3]^{0/+}$ species have had as starting materials for the synthesis of large Mn clusters, complex **3** may represent a new and alternative route to Mn complexes with novel magnetic properties. Spin density calculations on **3** suggest that, in the case of a Jahn–Teller distorted Mn^{III} ion, the elongated axis may favour a spin delocalisation mechanism.

Experimental Section

$[Mn_{26}O_{17}(OH)_8(OMe)_4F_{10}(bta)_{22}(MeOH)_{14}(H_2O)_2]\cdot MeOH$ (1·MeOH)

Method A: Anhydrous MnF_3 (0.5 g) and benzotriazole (3 equiv, btaH, 1.6 g) were ground together and placed in a Schlenk tube under an inert atmosphere and heated at 100 °C for 30 min. The resulting black "melt" was dried in vacuo and allowed to cool to form a black solid. The solid was dissolved in MeOH (20 mL at 50 °C) to result in a black solution from which black crystals of **1** were obtained after 2 weeks upon diffusion of Et_2O. Yield: 10 %.

Method B: Anhydrous MnF_3 (0.5 g) and benzotriazole (btaH, 3 equiv, 1.6 g) were heated in methanol (20 mL) at 50 °C under aerobic conditions for 10 min. The resulting black solution was filtered, and black crystals of **1** were obtained after 2 weeks upon diffusion of Et_2O. Yield: 15 %; IR (KBr): $\tilde{\nu}=1654$ (w), 1637 (w), 1617 (w), 1570 (w), 1560 (w), 1542 (w), 1508 (w), 1490 (w), 1442 (m), 1374 (w), 1294 (w), 1269 (m), 1225 (m), 1146 (m), 1017 (w), 990 (w), 920 (w), 792 (s), 747 (s), 643 (m), 580 cm^{-1} (w); elemental analysis calcd (%) for $C_{151}H_{172}N_{66}O_{46}F_{10}Mn_{26}$: C 34.44, H 3.29, N 17.56, F 3.61; found: C 34.65, H 3.09, N 17.89, F 3.55.

$[Mn_{10}O_6(OH)_2(bta)_8(py)_8F_8]\cdot 0.75\,H_2O\cdot 0.5\,btaH\cdot 1.4\,CH_3OH$ ($2\cdot 0.75\,H_2O\cdot 0.5\,btaH\cdot 1.4\,CH_3OH$): Anhydrous MnF_3 (0.5 g) and benzotriazole (btaH, 3 equiv, 1.6 g) were heated in methanol (20 mL) at 50 °C under aerobic conditions for 10 min. The resulting black solution was filtered, and pyridine (1.00 mL) was added dropwise. Black crystals of **2** were obtained after 2 weeks upon diffusion of Et_2O into the solution. Yield: 20 %; IR (KBr): $\tilde{\nu}=1599$ (s), 1570 (w), 1487 (w), 1443 (s), 1290 (w), 1217 (m), 1130 (m), 1068 (w), 1036 (w), 1008 (w), 990 (w), 917 (w), 791 (m), 749 (s), 699 (s), 641 (m), 603 (m), 564 cm^{-1} (w); elemental analysis calcd (%) for $C_{88}H_{74}N_{32}O_8F_8Mn_{10}$: C 43.87 H 3.10, N 18.60, F 6.30; found C 43.58, H 2.88, N 17.98, F 6.45.

$[NHEt_3]_2[Mn_3O(bta)_6F_3]\cdot 2\,MeOH$ (3·2 MeOH): Anhydrous MnF_3 (0.5 g) and benzotriazole (btaH, 3 equiv, 1.6 g) were heated in methanol (20 mL) at 50 °C under aerobic conditions for 10 min. The resulting black solution was filtered, and triethylamine was (0.33 mL) added. Upon evaporation in air, green crystals of **3** were obtained after 24 h. Yield: 80 %; IR (KBr): $\tilde{\nu}=1609$ (s), 1572 (s), 1485 (m), 1444 (s), 1390 (w), 1321 (w), 1283 (w), 1265 (w), 1219 (m), 1129 (m), 1104 (m), 1035 (w), 992 (w), 916 (w), 785 (m), 752 (s), 660 (s), 639 (m), 571 (w), 554 cm^{-1} (m); elemental analysis calcd (%) for $C_{49}H_{60}N_{20}O_2F_3Mn_3$: C 50.09, H 4.90, N 24.34, F 4.82, Mn 14.32; found C 49.50, H 5.01, N 24.04, F 4.78, Mn 14.55. **X-ray crystallography**: Crystallographic data for **1**–**3** are collected in Table 1.

*Crystal data for **1***: Synchrotron radiation (CCLRC Daresbury Laboratory, Station 9.8, $\lambda=0.6867$ Å) Bruker AXS SMART 1 K CCD diffractometer,[17] narrow frame ω rotations, and corrected semi-empirically for absorption and incident beam decay (transmission 0.88–0.97).

*Crystal data for **2***: Synchrotron radiation (CLRC Daresbury Laboratory, Station 9.8, $\lambda=0.6867$ Å) Bruker AXS SMART 1 K CCD diffractometer,[17] narrow frame ω rotations, and corrected semi-empirically for absorption and incident beam decay (transmission 0.88–0.97).

*Crystal data for **3***: A Bruker SMART APEX CCD diffractometer, $\lambda=0.71073$ Å with 0.3° ω frame rotations.

CCDC-194440 (**1**), CCDC-234429 (**2**) and CCDC-234430 (**3**) contain the supplementary crystallographic data for this paper. These data can be obtained free of charge via www.ccdc.cam.ac.uk/conts/retrieving.html (or from the Cambridge Crystallographic Data Centre, 12 Union Road, Cambridge CB2 1EZ, UK; fax: (+44) 1223-336033; or deposit@ccdc.cam.uk).

Magnetic measurements: Variable-temperature, solid-state direct current (DC) magnetic susceptibility data down to 1.80 K were collected on a Quantum Design MPMS-XL SQUID magnetometer equipped with a 7 T DC magnet at the University of Florida. Diamagnetic corrections were applied to the observed paramagnetic susceptibilities using Pascal's constants. The DC measurements below 1.80 K were performed on single crystals by using an array of micro-SQUIDS.[18]

Acknowledgement

This work was supported by Lloyd's of London Tercentenary Foundation, the EPSRC and the NSF. We would also like to thank the EPSRC-UKCCF for computer time on the Columbus system, and CCLRC for access to Station 9.8 for data collection.

[1] *Manganese Redox Enzymes* (Ed.: V. L. Pecoraro), VCH, Weinheim, **1992**.

[2] N. A. Law, M. T. Caudle, V. L. Pecoraro. *Advances in Inorganic Chemistry* (Ed.: A. G. Sykes), Academic Press, London, **1998**, *46*, 305.

[3] a) J. B. Vincent, C. Christmas, H-R Chang, Q. Li, P. D. W. Boyd, J. C. Huffman, D. N. Hendrickson, G. Christou, *J. Am. Chem. Soc.* **1989**, *111*, 2086; b) S. Wang, H.-L. Tsai, K. S. Hagen, D. N Hendrickson, G. Christou, *J. Am. Chem. Soc.* **1994**, *116*, 8376.
[4] See, for example a) E. K. Brechin, M. Soler, G. Christou, J. Davidson, D. N. Hendrickson, S. Parsons, W. Wernsdorfer, *Polyhedron* **2003**, *22*, 1771; b) E. K. Brechin, M. Soler, G. Christou, M. Helliwell, S. J. Teat, W. Wernsdorfer, *Chem. Commun.* **2003**, 1276.
[5] R. Sessoli, D. Gatteschi, D. N. Hendrickson, G. Christou, *MRS Bull.* **2000**, *25*, 66.
[6] a) R. Sessoli, H.-L. Tsai, A. R. Schake, S. Wang, J. B. Vincent, K. Folting, D. Gatteschi, G. Christou, D. N. Hendrickson, *J. Am. Chem. Soc.* **1993**, *115*, 1804; b) R. Sessoli, D. Gatteschi, A. Caneschi, M. A. Novak, *Nature* **1993**, *365*, 141.
[7] M. Soler, W. Wernsdorfer, K. Folting, M. Pink, G. Christou, *J. Am. Chem. Soc.* **2004**, *126*, 2156, and references therein; A. J. Tasiopolous, A. Vinslava, W. Wernsdorfer, K. A. Abboud, G. Christou, *Angew. Chem.* **2004**, *116*, 2169; *Angew. Chem. Int. Ed.* **2004**, *43*, 2117.
[8] D. N. Hendrickson, G. Christou, H. Ishimoto, J. Yoo, E. K. Brechin, A. Yamaguchi, E. M. Rumberger, S. M. J. Aubin, Z. Sun, G. Aromí, *Polyhedron* **2001**, *20*, 1479.
[9] See, for example: E. K. Brechin, C. Boskovic, W. Wernsdorfer, J. Yoo, A. Yamaguchi, E. C. Sanudo, T. R. Concolino, A. L. Rheingold, H. Ishimoto, D. N. Hendrickson, G. Christou, *J. Am. Chem. Soc.* **2002**, *124*, 9710.
[10] I. Dugdale, J. B. Cotton, *Corros. Sci.* **1963**, *3*, 69.
[11] V. Tangoulis, C. P. Raptopoulou, A. Terzis, E. G. Bakalbassis, E. Diamontopoulos, S. P. Perlepes, *Mol. Cryst. Liq. Cryst.* **1999**, *335*, 463.
[12] D. M. Low, L. F. Jones, A. Bell, E. K. Brechin, T. Mallah, E. Rivière, S. J. Teat, E. J. L. McInnes, *Angew. Chem.* **2003**, *115*, 3911; *Angew. Chem. Int. Ed.* **2003**, *42*, 3781.
[13] a) N. V. Gerbeleu, Y. T. Struchkov, G. A. Timco, A. S. Batsanov, K. M. Indrichan, G. A. Popovic, *Dokl. Chem.* **1991**, *313*, 232; b) N. V. Gerbeleu, Y. T. Struchkov, G. A Timco, A. S. Batsanov, K. M. Indrichan, G. A Popovic, *Dokl. Akad. Nauk SSSR* **1991**, *313*, 1459.
[14] A. Bino, M. Ardon, D. Lee, B. Spingler, S. J. Lippard, *J. Am. Chem. Soc.* **2002**, *124*, 4578.
[15] L. F. Jones, E. K. Brechin, D. Collison, A. Harrison, S. J. Teat, W. Wernsdorfer, *Chem. Commun.* **2002**, 2974.
[16] F. K. Larsen, J. Overgaard, S. Parsons, E. Rentschler, A. A. Smith, G. A. Timco, R. E. P. Winpenny, *Angew. Chem.* **2003**, *115*, 6160; *Angew. Chem. Int. Ed.* **2003**, *42*, 5978.
[17] J. Cernik, W. Clegg, C. R. A. Catlow, G. Bushnell-Wye, J. V. Flaherty, G. N. Greaves, I. Burrows, D. J. Taylor, S. J. Teat, M. Hamichi, *J. Synchrotron Radiat.* **1997**, *4*, 279–286; SMART version 5.054, Bruker AXS Madison, WI (USA), **1998**; SAINT version 6.02a, Bruker-AXS, Madison, WI (USA), **2000**; G. M. Sheldrick, SADABS, Program for scaling and correction of area detector data, University of Gottingen (Germany), **1997**; G. M. Sheldrick, SHELXTL, version 5.10, Bruker AXS, Madison, WI (USA), **2000**.
[18] W. Wernsdorfer, *Adv. Chem. Phys.* **2001**, *118*, 99.
[19] MAGNET, E. R. Davidson, Indiana University.
[20] See, for example: C. Boskovic, W. Wernsdorfer, K. Folting, D. N. Hendrickson, G. Christou, *Inorg. Chem.* **2002**, *41*, 5107.
[21] L. Thomas, A. Caneschi, B. Barbara, *Phys. Rev. Lett.* **1999**, *83*, 2398.
[22] J. B. Vincent, H.-R. Chang, K. Folting, J. C. Huffman, G. Christou, D. N. Hendrickson, *J. Am. Chem. Soc.* **1987**, *109*, 5703.
[23] K. Wieghardt, U. Bossek, B. Nuber, J. Weiss, J. Bonvoisin, M. Corbella, S. Vitols, J. J. Girerd, *J. Am. Chem. Soc.* **1988**, *110*, 7398.
[24] L. Noodleman, *J. Chem. Phys.* **1981**, *74*, 5737.
[25] a) E. Ruiz, S. Alvarez, J. Cano, P. Alemany, *J. Comput. Chem.* **1999**, *20*, 1391; E. Ruiz, A. R. Fortea, J. Cano, S. Alvarez, P. Alemany, *J. Comput. Chem.* **2003**, *24*, 982; E. Ruiz, J. Cano, S. Alvarez, A. Caneschi, D. Gatteschi, *J. Am. Chem. Soc.* **2003**, *125*, 6791; A. Abu-Nawwas, J. Cano, P. Christian, T. Mallah, G. Rajaraman, S. J Teat, R. E. P. Winpenny, Y. Yukawa, *Chem. Commun.* **2004**, 314; b) P. Christian, G. Rajaraman, A. Harrison, J. J. W. McDouall, J. Raftery, R. E. P. Winpenny, *J. Chem. Soc. Dalton Trans.* **2004**, 1511.
[26] E. Ruiz, A. R. Fortea, J. Cano, S. Alvarez, P. Alemany, *J. Comput. Chem.* **2003**, *24*, 982; E. Ruiz, J. Cano, S. Alvarez, A. Caneschi, D. Gatteschi, *J. Am. Chem. Soc.* **2003**, *125*, 6791; E. Ruiz, S. Alvarez, A. Rodriguez-Fortea, P. Alemany, Y. Pouillon, C. Massobrio in *Magnetism: Molecules to Materials Vol. II* (Eds.: J. S. Miller, M. Drillon), Wiley-VCH, Weinheim, **2001**; G. Rajaraman, J. Cano, E. K. Brechin, E. J. L. McInnes, *Chem. Commun.* **2004**, 1476.
[27] Gaussian 98, Revision A.11.3, M. J. Frisch, G. W. Trucks, H. B. Schlegel, G. E. Scuseria, M. A. Robb, J. R. Cheeseman, V. G. Zakrzewski, J. A. Montgomery, Jr., R. E. Stratmann, J. C. Burant, S. Dapprich, J. M. Millam, A. D. Daniels, K. N. Kudin, M. C. Strain, O. Farkas, J. Tomasi, V. Barone, M. Cossi, R. Cammi, B. Mennucci, C. Pomelli, C. Adamo, S. Clifford, J. Ochterski, G. A. Petersson, P. Y. Ayala, Q. Cui, K. Morokuma, N. Rega, P. Salvador, J. J. Dannenberg, D. K. Malick, A. D. Rabuck, K. Raghavachari, J. B. Foresman, J. Cioslowski, J. V. Ortiz, A. G. Baboul, B. B. Stefanov, G. Liu, A. Liashenko, P. Piskorz, I. Komaromi, R. Gomperts, R. L. Martin, D. J. Fox, T. Keith, M. A. Al-Laham, C. Y. Peng, A. Nanayakkara, M. Challacombe, P. M. W. Gill, B. Johnson, W. Chen, M. W. Wong, J. L. Andres, C. Gonzalez, M. Head-Gordon, E. S. Replogle, and J. A. Pople, Gaussian, Inc., Pittsburgh PA, **2002**.
[28] J. K. McCusker, H. G. Jang, S. Wang, G. Christou, D. N. Hendrickson, *Inorg. Chem.* **1992**, *31*, 1874.
[29] J. Cano, E. Ruiz, S. Alvarez, M. Verdaguer, *Comments Inorg. Chem.* **1998**, *20*, 27.

Received: March 29, 2004
Published online: September 13, 2004